On the mechanics of strain localization in plasticity: Isotropic and orthotropic, elasto- and rigid-plastic, associated and non-associated models

Miguel Cervera[a], Jian-Ying Wu[b,*], Sungchul Kim[a], Michele Chiumenti[a]

[a] *CIMNE, Technical University of Catalonia, Edificio C1, Campus Norte, Jordi Girona 1-3, 08034 Barcelona, Spain.*
[b] *State Key Laboratory of Subtropic Building Science, South China Univeristy of Technology, 510641 Guangzhou, China.*

Abstract

As strain localization is usually prognostics of localized failure in solids and structures, prediction of its occurrence and quantification of its adverse effects are of both theoretical and practical significance. Regarding plastic solids, onset of strain localization was presumed to be coincident with strain bifurcation, and the discontinuous bifurcation analysis was usually adopted to determine the discontinuity orientation though it does not apply to rigid-plastic solids. However, recent studies indicate that strain bifurcation and localization correspond to distinct stages of localized failure and should be dealt with separately. In this work the mechanics of strain localization is addressed for perfect and softening plasticity in the most general context. Both isotropic and orthotropic, elasto- and rigid-plastic solids with associated and non-associated flow rules are analytically considered and numerically validated, extending our previous work on softening plasticity with associated evolution laws. In addition to Maxwell's kinematics and continuity of the traction rate for strain bifurcation, a novel necessary condition, i.e., the stress rate objectivity (independent from the discontinuity bandwidth), and the resulting kinematic and static constraints, are derived for the occurrence of strain localization. In particular, the localization angles of the discontinuity band (surface) depend only on the specific stress state and the plastic flow tensor, relevant neither to the material elastic constants nor to the plastic yield function. Moreover, it is found that a transition stage generally exists in the case of plane strain during which the orientation of plastic flow rotates progressively such that strain localization may occur. Back-to-back numerical predictions of some benchmark problems, involving both perfect and softening plasticity, sufficiently justify the analytical results.

Keywords:
Localized failure, plasticity, strain localization, strain bifurcation, discontinuities.

1. Introduction

As a typical phenomenon of localized failure in solids and structures, strain localization is manifested by highly non-uniform deformations concentrated within narrow bands of dimensions much smaller than the structural size. It leads to strain (weak) or even displacement (strong) discontinuities across the localization band, triggering substantial

*Corresponding author
Email address: jywu@scut.edu.cn (Jian-Ying Wu)

loss of integrity and safety or even collapse of structures. Consequently, quantification of strain localization is of both theoretical and practical significance in the prevention of localized failure for structural designs.

Historically, studies in strain localization originally stem from the interest in uncovering the mechanisms of shear banding in cohesive-frictional (associated and non-associated) geotechnical materials like soils (Mohr, 1900; Prandtl, 1920; Hill, 1958) and of extrusion and necking in bulk and sheet metal forming (Hill, 1948). For the sake of brevity, in this work the material is assumed to be perfectly homogeneous; that is, only strain localization occurring spontaneously is considered. This is different from the Marciniak and Kuczyński (1967) criterion, widely-adopted in the field of sheet metal forming, in which strain localization is initiated by a pre-existing geometric and/or structural non-homogeneity (Rojek et al., 2004; Lumelskyj et al., 2019; Banabic et al., 2021).

In the context of shear-driven "slip lines" in pressure independent rigid-plastic solids, strain localization was studied in the seminal works of Prandtl (1920); Hencky (1923, 1924); Mandel (1942). This problem was later revisited by Hill (1950) and the "slip lines" were interpreted as the characteristic lines of the underlying governing equations of hyperbolic type. In these early works, only rigid-plasticity with no elastic deformations was considered, and incompressible behavior prior to shear-driven plastic yielding was assumed.

Strain localization in elastoplastic solids was later investigated by Hill (1958, 1962); Thomas (1961); Rice (1968) as a bifurcation problem. Upon the assumption of linear comparison (artificial) solids (i.e., plastic loading both inside and outside the discontinuity band), a strain bifurcation condition, i.e., singularity of the elastoplastic acoustic tensor, is derived from the combination of Maxwell's kinematics and traction rate continuity condition across the discontinuity band. One noteworthy result is that strain bifurcation always occurs at the hardening stages, i.e., $H_b \geq 0$, for non-associated plastic materials (Rudnicki and Rice, 1975). Moreover, closed-form results for the discontinuity orientation and the associated hardening/softening moduli were obtained for the 2-D plane stress and plane strain conditions (Runesson et al., 1991). In the computational context, the above bifurcation condition with null hardening modulus was recommended to determine the discontinuity orientation in embedding weak or strong discontinuities into finite elements (Simó et al., 1993; Oliver, 1996; Oliver et al., 1999).

Though the above bifurcation analysis has been widely adopted, two issues cannot be overlooked. On the one hand, the strain bifurcation analysis does not apply to rigid-plastic solids since there is no elastic strain and the stiffness tensor is undetermined. Consequently, the stress cannot be directly given from the elastoplastic constitutive relation, and the elastoplastic acoustic tensor is no longer well-defined. This makes unseemly the strain bifurcation analysis in rigid-plastic solids since it cannot be formulated as an equilibrium/stiffness problem.

On the other hand, the elastoplastic acoustic tensor depends on the hardening/softening modulus H, so do the bifurcation condition and the resulting discontinuity orientation. As clarified in Rice and Rudnicki (1980); Borré and Maier (1989), for the more frequently encountered incrementally nonlinear (real) material (i.e., inelastic loading inside the discontinuity band and elastic unloading outside it) the standard bifurcation analysis gives only the upper bound of strain localization. That is, though the initial bifurcation point corresponding to the largest hardening/softening modulus H_b can be uniquely determined, strain localization is still indefinite and it can occur at any instant for

$H \leq H_b$. Moreover, even if the hardening/softening modulus H is specified *a priori* in an *ad hoc* manner, there may exist several solutions that fulfill the bifurcation condition. For instance, regarding the non-associated Mohr elastoplastic material, at least two valid solutions, one corresponding to Mohr's solution (Mohr, 1900) and the other to Roscoe's solution (Roscoe, 1970), exist at the peak of the stress – strain relation ($H = 0$); see Ottosen and Runesson (1991). Consequently, if the discontinuity orientation is fixed at such detected bifurcation points, it is unavoidable to get pathological results in the computational context (Oliver et al., 1999). In particular, stress locking occurs due to the mis-prediction of the discontinuity orientation (Oliver et al., 2012).

As the standard bifurcation analysis is not sufficient to determine the occurrence of strain localization, a more stringent condition needs to be introduced. To this end, the authors (Cervera et al., 2012) proposed using the stress (rate) boundedness condition to determine the discontinuity orientation of associated von Mises (J_2) plastic materials. This condition was extended to isotropic elastoplastic models with general failure criteria (e.g., Rankine, von Mises, Mohr-Coulomb, Drucker-Prager, and other more complex ones) (Wu and Cervera, 2014, 2015, 2016), to orthotropic plastic ones (Cervera et al., 2020; Kim et al., 2021), and also to strain-based damage models (Wu and Cervera, 2017). Not only the discontinuity orientation but also the localized model upon strain localization, i.e., constitutive relations, evolution equations, traction-based failure criterion, softening functions, etc., can be determined consistently from a given material model (Wu and Cervera, 2015, 2016).

For the case of inelastic loading inside the discontinuity band and elastic unloading outside it, the stress (rate) boundedness condition is more constrictive than the traction (rate) continuity adopted in the strain bifurcation one. Remarkably, for isotropic and orthotropic elasto-plastic materials with associated evolution laws, the discontinuity orientation predicted from the stress (rate) boundedness condition depends exclusively on the plastic flow tensor, independent of the elastic properties and the hardening/softening modulus. This is contradicting from the predictions given by the strain bifurcation condition. Extensive numerical simulations (Cervera et al., 2012, 2015; Li et al., 2018; Cervera et al., 2020) confirmed the analytical solutions with no *a priori* known information in the finite element simulations. These numerical results justify the stress (rate) boundedness condition for strain localization in plastic solids with associated flow rules and under the loading/unloading scenarios. Nevertheless, the not unusual loading/loading scenarios and the practically more encountered non-associated plastic flow rules remain to be investigated.

In this work the mechanics of strain localization is addressed in the more general cases. Isotropic and orthotropic, rigid-plastic or elastoplastic solids with associated or non-associated evolution laws are analytically considered and numerically validated, extending our previous work on softening plasticity with associated evolution laws. An extra necessary condition, i.e., the stress rate objectivity (independent of the discontinuity bandwidth), in addition to Maxwell's kinematics and continuity of the traction (rate) for strain bifurcation, is postulated for the occurrence of strain localization in perfectly or softening plastic solids. Both the loading/unloading and loading/loading scenarios are accounted for. This incorporates the "slip-line" or "zero rate of extension" for rigid-plastic solids (Hill, 1950) and elastoplastic soils (Roscoe, 1970) as particular cases. Moreover, the previously proposed stress rate boundedness condition is also recovered as a particular case of strong discontinuities or regularized ones with a vanishing bandwidth,

respectively, under the loading/unloading scenario.

The remainder of this paper is structured as follows. Section 2 presents briefly the kinematics, constitutive relations and statics for the analysis of strain localization. Section 3 is devoted the mechanics of strain localization in the continuum setting. Plastic yielding, strain bifurcation and strain localization are regarded as distinct stages of the whole failure process of elasto- and rigid-plastic solids. The difference and correlation between stain bifurcation and strain localization is discriminated. The analytical results for the localization angles in 2-D plane stress and plane strain conditions are also presented. Numerical validation of the proposed strain localization condition and the derived analytical results is addressed in Section 4 using the stabilized mixed $\boldsymbol{u}/p$ finite elements, regarding the von Mises and Hill models with associated and non-associated plastic flow rules. A horizontal slit under vertical stretch and the Prandtl punch test, are further considered in Section 5, further justifying the proposed condition for strain localization. The most relevant conclusions are drawn in Section 6 to close the paper.

2. General setting of discontinuities

Let us consider the reference configuration of an inelastic (elasto- and rigid-plastic in this work) solid $\Omega \subset \mathbb{R}^{n_{\rm dim}}$ ($n_{\rm dim} = 1, 2, 3$). The external boundary is denoted by $\partial\Omega \subset \mathbb{R}^{n_{\rm dim}-1}$, with $\boldsymbol{n}^*$ being the outward unit normal vector. Deformations of the solid are characterized by the displacement field $\boldsymbol{u}(\boldsymbol{x})$ and infinitesimal strain field $\boldsymbol{\epsilon}(\boldsymbol{x}) := \nabla^{\rm sym}\boldsymbol{u}(\boldsymbol{x})$, for the symmetric gradient operator $\nabla^{\rm sym}(\cdot)$ with respect to the spatial coordinate $\boldsymbol{x}$. Prescribed displacements $\boldsymbol{u}^*(\boldsymbol{x})$ and tractions $\boldsymbol{t}^*(\boldsymbol{x})$ are applied to two disjointed parts $\partial\Omega_u$ and $\partial\Omega_t$ of the boundary $\partial\Omega$, respectively. The distributed body forces (per unit volume) are denoted by $\boldsymbol{b}^*$. It is assumed in this work that only small deformations occur prior to strain localization; the extension to finite deformations in e.g., soft materials, can be addressed with analogous hypotheses in the appropriate kinematic and constitutive frameworks.

2.1. Kinematics of discontinuities

Initially both the displacement and strain fields are continuous everywhere in the solid. In this case, the standard kinematics applies. Upon a specific condition and thereafter, either a discontinuity band or a discontinuity surface may form, depending on the localization band width. A discontinuity band can be regarded as a geometric regularization of a discontinuity surface (line) while the latter is recovered as bandwidth of the former vanishes in the limit.

2.1.1. Discontinuity band

As shown in Fig. 1(a), let us first consider the discontinuity band $\mathcal{B}$ of a finite width $b \ll L$, with L being the structural characteristic length. Note that in the continuum setting the bandwidth b is a numerical regularization parameter so that its value can be taken as small as possible. In the discrete (finite element) setting, b may be dependent on the mesh resolution. The discontinuity band $\mathcal{B}$ is delimited by two parallel surfaces $\mathcal{S}^+$ and $\mathcal{S}^-$, with the center one denoted by $\mathcal{S}$, i.e., $\Omega^+ \cup \Omega^- \cup \mathcal{B} = \Omega$. Let (n, m, t) be a set of orthogonal local axes, with $\boldsymbol{n}_{\mathcal{S}}$, $\boldsymbol{m}_{\mathcal{S}}$ and $\boldsymbol{t}_{\mathcal{S}}$ being the normal vector, the in-plane and out-of-plane tangential ones of the surface $\mathcal{S}$, respectively.

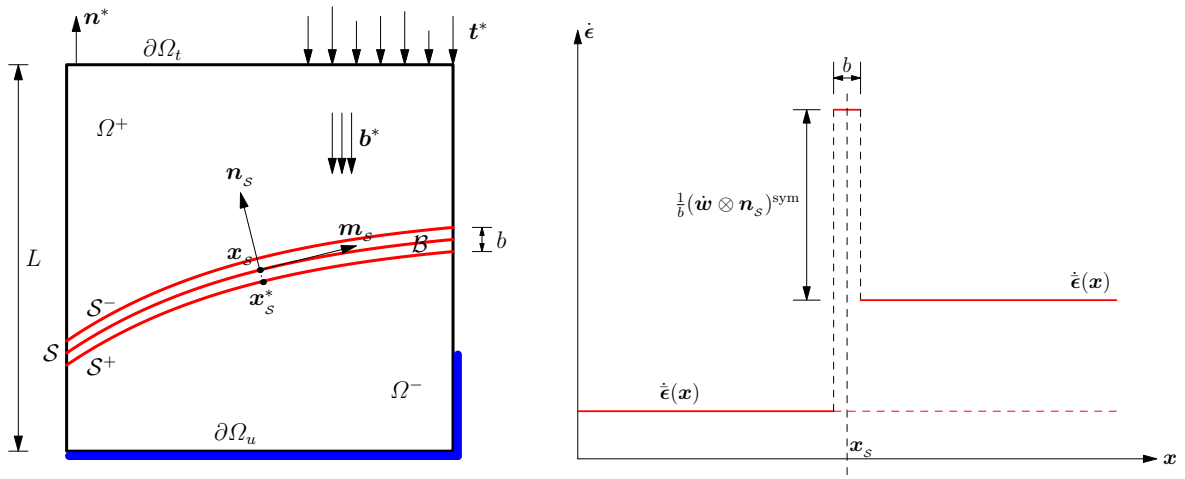

(a) A discontinuity band

(b) Kinematics of the discontinuity band

Figure 1: An inelastic solid with a discontinuity band.

In this case, the displacement rate (velocity) field $\dot{\boldsymbol{u}}(\boldsymbol{x})$ is continuous, with an apparent velocity jump $\dot{\boldsymbol{w}} := \dot{\boldsymbol{u}}(\boldsymbol{x} \in \Omega^+ \cap \mathcal{S}^+) - \dot{\boldsymbol{u}}(\boldsymbol{x} \in \Omega^- \cap \mathcal{S}^-)$ across the discontinuity band $\mathcal{B}$, where $\dot{(\cdot)}$ signifies the time derivative. The resulting strain rate field can be given by

$$\dot{\boldsymbol{\epsilon}}(\boldsymbol{x}) = \dot{\bar{\boldsymbol{\epsilon}}}(\boldsymbol{x}) + \dot{\tilde{\boldsymbol{\epsilon}}}(\boldsymbol{x}), \qquad \dot{\tilde{\boldsymbol{\epsilon}}}(\boldsymbol{x}) = \frac{1}{b}\big(\dot{\boldsymbol{w}} \otimes \boldsymbol{n}_{\mathcal{S}}\big)^{\text{sym}}\, \Xi_{\mathcal{B}}(\boldsymbol{x}) \tag{2.1}$$

for the collocation function $\Xi_{\mathcal{B}}(\boldsymbol{x})$ within the discontinuity band $\mathcal{B}$

$$\Xi_{\mathcal{B}}(\boldsymbol{x}) = \begin{cases} 1 & \boldsymbol{x} \in \mathcal{B} \\ 0 & \boldsymbol{x} \in \Omega \backslash \mathcal{B} \end{cases} \tag{2.2}$$

Note that the strain rate field $\dot{\bar{\boldsymbol{\epsilon}}}(\boldsymbol{x})$ outside the discontinuity band $\mathcal{B}$ is independent of the bandwidth b, while the magnitude of the localized one $\dot{\tilde{\boldsymbol{\epsilon}}}$ is inversely proportional to it: the smaller the bandwidth b is, the larger the localized strain becomes; see Figure 1(b). Hereafter, the bar-symbols $\bar{(\cdot)}$ are associated with the material points outside the discontinuity band (surface).

Remark 2.1 Note that in the kinematics (2.1) the collocation function $\Xi_{\mathcal{B}}(\boldsymbol{x})$ can be replaced by a bell-shaped continuous function localized within the discontinuity band $\mathcal{B}$. In this case the localized strain rate $\dot{\tilde{\boldsymbol{\epsilon}}}(\boldsymbol{x})$ is continuous across the localization band, but it is still inversely proportional to the bandwidth b. □

2.1.2. Discontinuity surface

As mentioned, the bandwidth b is a numerical parameter that can be made as small as desired. In the limit case $b \to 0$, the discontinuity band $\mathcal{B}$ becomes a discontinuity surface $\mathcal{S}$. It then follows that

$$\lim_{b\to 0} \frac{1}{b}\Xi_{\mathcal{B}}(\boldsymbol{x}) = \delta_{\mathcal{S}}(\boldsymbol{x}) = \begin{cases} +\infty & \boldsymbol{x} \in \mathcal{S} \\ 0 & \boldsymbol{x} \in \Omega \backslash \mathcal{S} \end{cases} \tag{2.3}$$

for the Dirac-delta $\delta_{\mathcal{S}}(\boldsymbol{x})$ defined at the discontinuity surface $\mathcal{S}$.

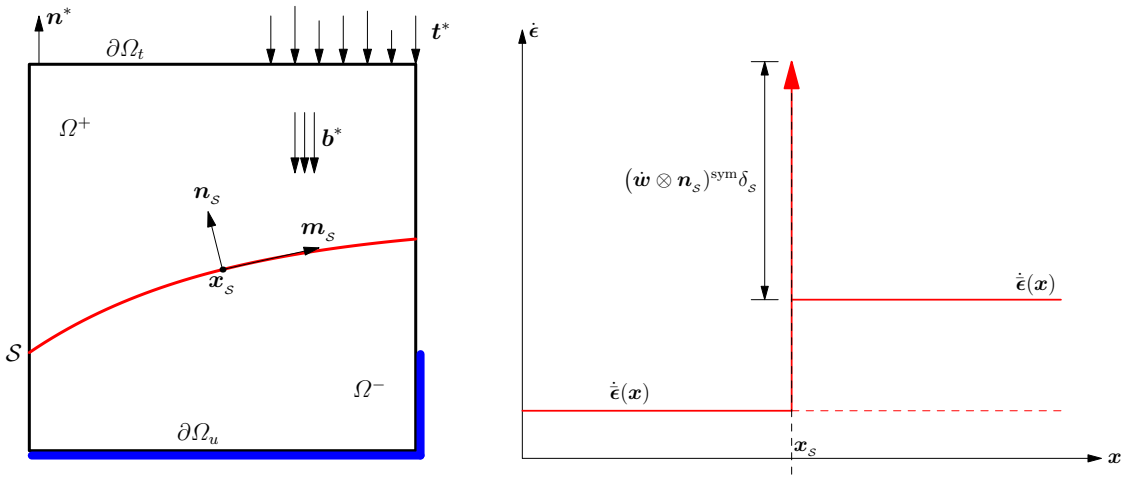

(a) A discontinuity surface (b) Kinematics of the discontinuity surface

Figure 2: An inelastic solid with a discontinuity surface.

Accordingly, the strain rate field becomes singular

$$\dot{\boldsymbol{\epsilon}}(\boldsymbol{x}) = \dot{\bar{\boldsymbol{\epsilon}}}(\boldsymbol{x}) + \dot{\tilde{\boldsymbol{\epsilon}}}(\boldsymbol{x}), \qquad \dot{\tilde{\boldsymbol{\epsilon}}}(\boldsymbol{x}) = \big(\dot{\boldsymbol{w}} \otimes \boldsymbol{n}\big)^{\mathrm{sym}}\, \delta_{\mathcal{S}}(\boldsymbol{x}) \tag{2.4}$$

Similarly, the strain rate field $\dot{\bar{\boldsymbol{\epsilon}}}(\boldsymbol{x})$ outside the discontinuity band $\mathcal{B}$ is independent of the bandwidth b, while the localized one $\dot{\tilde{\boldsymbol{\epsilon}}}(\boldsymbol{x})$ is singular. The above kinematics is shown in Figure 2.

Remark 2.2 As the discontinuity surface can be recovered from the discontinuity band upon a vanishing bandwidth $b \to 0$, hereafter only the kinematics of the discontinuity band is considered. □

2.2. Elastoplastic stress–strain relations

For elastoplastic models, the constitutive relation is expressed in rate form as

$$\dot{\boldsymbol{\epsilon}} = \dot{\boldsymbol{\epsilon}}^e + \dot{\boldsymbol{\epsilon}}^p, \qquad \dot{\boldsymbol{\sigma}} = \mathbb{E}_0 : \dot{\boldsymbol{\epsilon}}^e = \mathbb{E}_0 : \big(\dot{\boldsymbol{\epsilon}} - \dot{\boldsymbol{\epsilon}}^p\big) \tag{2.5}$$

where the second-order tensors $\boldsymbol{\sigma}$ and $\boldsymbol{\epsilon}$ represent the stress and strain, respectively, with $\boldsymbol{\epsilon}^e$ and $\boldsymbol{\epsilon}^p$ being the elastic and plastic parts of the latter; the fourth-order material elasticity tensor $\mathbb{E}_0$ can be either isotropic or orthotropic.

Without loss of generality, the plastic strain rate is given by the following evolution laws

$$\dot{\boldsymbol{\epsilon}}^p = \dot{\lambda}\boldsymbol{\Lambda}^p, \qquad \dot{\kappa} = \dot{\lambda} h^p \tag{2.6}$$

for the plastic multiplier $\dot{\lambda}$ satisfying the classical Karush-Kuhn-Tucker conditions

$$\dot{\lambda} \geq 0, \qquad f(\boldsymbol{\sigma}, q) \leq 0, \qquad \dot{\lambda} f(\boldsymbol{\sigma}, q) \equiv 0 \tag{2.7}$$

where a stress-based yield function $f(\boldsymbol{\sigma}, q) \leq 0$, with q being the stress-like internal variable (yield stress) conjugate to the strain-like one κ which measure the plastic state, is introduced. The flow tensor $\boldsymbol{\Lambda}^p := \partial f^p / \partial \boldsymbol{\sigma}$ and the derivative $h^p := -\partial f^p / \partial q$ are normal to the potential function $f^p(\boldsymbol{\sigma}, q)$ — if the latter is identical (or more generally, proportional) to the yield function $f(\boldsymbol{\sigma}, q)$, the plastic flow is associated, and is non-associated otherwise. In absence of plastic flow or in the case of elastic unloading, i.e., $\dot{\lambda} = 0$, the yield condition is not activated, i.e., $f(\boldsymbol{\sigma}, q) < 0$; otherwise, plastic flow occurs. In this work, both perfect plasticity and softening one are addressed.

2.3. Statics of discontinuities

For elastoplastic solids, the stress rates inside the discontinuity band (surface) and outside it are given by

$$\dot{\boldsymbol{\sigma}} = \mathbb{E}_0 : \left(\dot{\boldsymbol{\epsilon}} - \dot{\boldsymbol{\epsilon}}^p\right) = \mathbb{E}_0 : \left(\dot{\boldsymbol{\epsilon}} - \dot{\lambda}\boldsymbol{\Lambda}^p\right) \tag{2.8a}$$

$$\dot{\bar{\boldsymbol{\sigma}}} = \mathbb{E}_0 : \left(\dot{\bar{\boldsymbol{\epsilon}}} - \dot{\bar{\boldsymbol{\epsilon}}}^p\right) = \mathbb{E}_0 : \left(\dot{\bar{\boldsymbol{\epsilon}}} - \dot{\bar{\lambda}}\bar{\boldsymbol{\Lambda}}^p\right) \tag{2.8b}$$

where the elastoplastic relations (2.5) and (2.6) have been recalled for both material points inside and outside the discontinuity band.

Accordingly, the resulting jump in the stress rate, $[\![\dot{\boldsymbol{\sigma}}]\!]$, is expressed as

$$[\![\dot{\boldsymbol{\sigma}}]\!] := \dot{\boldsymbol{\sigma}} - \dot{\bar{\boldsymbol{\sigma}}} = \mathbb{E}_0 : \left([\![\dot{\boldsymbol{\epsilon}}]\!] - \dot{\lambda}\boldsymbol{\Lambda}^p + \dot{\bar{\lambda}}\bar{\boldsymbol{\Lambda}}^p\right) = \mathbb{E}_0 : \left[\frac{1}{b}\left(\dot{\boldsymbol{w}} \otimes \boldsymbol{n}\right)^{\text{sym}} - \dot{\lambda}\boldsymbol{\Lambda}^p + \dot{\bar{\lambda}}\bar{\boldsymbol{\Lambda}}^p\right] \tag{2.9}$$

where the following Maxwell's kinematic condition has been considered

$$[\![\dot{\boldsymbol{\epsilon}}]\!] := \dot{\boldsymbol{\epsilon}} - \dot{\bar{\boldsymbol{\epsilon}}} = \frac{1}{b}\left(\dot{\boldsymbol{w}} \otimes \boldsymbol{n}_{\mathcal{S}}\right)^{\text{sym}} \tag{2.10}$$

Equilibrium across the discontinuity band (surface) gives the following continuity condition of the traction rate

$$\boldsymbol{n}_{\mathcal{S}} \cdot [\![\dot{\boldsymbol{\sigma}}]\!] = \boldsymbol{0} \qquad \Longrightarrow \qquad [\![\dot{\boldsymbol{\sigma}}]\!] = \dot{\alpha}_{mm}\boldsymbol{m}_{\mathcal{S}} \otimes \boldsymbol{m}_{\mathcal{S}} + \dot{\alpha}_{tt}\boldsymbol{t}_{\mathcal{S}} \otimes \boldsymbol{t}_{\mathcal{S}} + \dot{\alpha}_{mt}\left(\boldsymbol{m}_{\mathcal{S}} \otimes \boldsymbol{t}_{\mathcal{S}}\right)^{\text{sym}} \tag{2.11}$$

where the scalars $\dot{\alpha}_{mm}$, $\dot{\alpha}_{tt}$ and $\dot{\alpha}_{mt}$ can be either dependent on or independent of the bandwidth b, according to the deformation stage and stress state. Therefore, though stress rate discontinuities may occur, they can take place only on the plane of the discontinuity surface $\mathcal{S}$.

Remark 2.3 For rigid-plastic solids, the elastic strain $\boldsymbol{\epsilon}^e$ vanishes such that

$$\dot{\boldsymbol{\epsilon}} = \dot{\boldsymbol{\epsilon}}^p = \dot{\lambda}\boldsymbol{\Lambda}^p \tag{2.12}$$

In this case the stress (rate) cannot be directly determined from the constitutive relation $(2.5)_2$. Consequently, only the compatibility condition, rather than the equilibrium one, applies to rigid-plastic solids. □

3. The mechanics of strain localization: Continuum setting

In this section the mechanics of strain localization in plasticity is addressed in the continuum setting. The kinematics of discontinuities in an inelastic solid is first considered. After the classical concepts of plastic yielding (PY) and strain bifurcation (SB) are recalled, strain localization (SL) is further elaborated to general plastic models with associated and non-associated evolution laws.

3.1. Plastic yielding (PY)

Plastic yielding implies termination of linear elastic behavior. Plastic yielding occurs when the yield condition $f(\boldsymbol{\sigma}, q) = 0$ is activated, i.e. $\dot{\lambda} > 0$. It then follows from the consistency condition $\dot{f} = 0$ that

$$\dot{\lambda} = \frac{\boldsymbol{\Lambda} : \mathbb{E}_0 : \dot{\boldsymbol{\epsilon}}}{\boldsymbol{\Lambda} : \mathbb{E}_0 : \boldsymbol{\Lambda}^p + h \cdot H \cdot h^p} \tag{3.1}$$

for the derivatives $\boldsymbol{\Lambda} := \partial f / \partial \boldsymbol{\sigma}$ and $h := -\partial f / \partial q$ of the yield function $f(\boldsymbol{\sigma}, q)$. Note that the hardening/softening modulus $H := \partial q / \partial \kappa$ is null for perfect plasticity and negative for softening one. Internal snap-back is ruled out *a priori* with satisfaction of the condition $H > H_c := -\boldsymbol{\Lambda} : \mathbb{E}_0 : \boldsymbol{\Lambda}^p / (h \cdot h^p)$.

The corresponding constitutive relation in rate form then reads

$$\dot{\boldsymbol{\sigma}} = \mathbb{E}_0 : \left(\dot{\boldsymbol{\epsilon}} - \dot{\boldsymbol{\epsilon}}^p \right) = \mathbb{E}^{ep} : \dot{\boldsymbol{\epsilon}} \tag{3.2}$$

where the fourth-order elastoplasticity tangent $\mathbb{E}^{ep}$ is expressed as

$$\mathbb{E}^{ep} = \mathbb{E}_0 - \frac{\mathbb{E}_0 : \boldsymbol{\Lambda}^p \otimes \boldsymbol{\Lambda} : \mathbb{E}_0}{\boldsymbol{\Lambda} : \mathbb{E}_0 : \boldsymbol{\Lambda}^p + h \cdot H \cdot h^p} \tag{3.3}$$

For non-associated plasticity, i.e., $\boldsymbol{\Lambda}^p \neq \boldsymbol{\Lambda}$, the material tangent is not of major symmetry.

3.2. Strain bifurcation (SB)

Upon strain bifurcation, the strains inside and outside a small subdomain starts deviating from each other, resulting in a discontinuity band with the strain rate jump given by Maxwell's kinematics (2.10).

In this case, the material points inside the discontinuity band are in plastic loading, whereas those outside it can be either in plastic loading or elastic unloading, leading to the following *continuous* and *discontinuous* bifurcation scenarios, respectively:

- Loading–loading (i.e., the material is in loading both inside and outside the discontinuity band) or continuous bifurcation, i.e., $\dot{\lambda} > 0$ and $\dot{\bar{\lambda}} > 0$. Maxwell's kinematics (2.10) and the traction (rate) continuity (2.11) give the following continuous bifurcation condition (Rice, 1976)

  $$\det \boldsymbol{Q}^{ep}(\boldsymbol{n}_s) = 0 \tag{3.4}$$

  for the elastoplastic acoustic tensor $\boldsymbol{Q}^{ep} := \boldsymbol{n}_s \cdot \mathbb{E}^{ep} \cdot \boldsymbol{n}_s$ related to some normal vector $\boldsymbol{n}_s$.

- Loading–unloading (i.e., the material is in loading inside the band and in elastic unloading outside it) or discontinuous bifurcation, i.e., $\dot{\lambda} > 0$ and $\dot{\bar{\lambda}} = 0$. Discontinuous strain bifurcation may occur provided the following condition holds (Rice and Rudnicki, 1980; Borré and Maier, 1989)

  $$\det \boldsymbol{Q}^{ep}(\boldsymbol{n}_s) \leq 0 \tag{3.5}$$

  for some normal vectors $\boldsymbol{n}_s$.

Note that the condition (3.4) of continuous bifurcation is the upper bound for that of discontinuous one (3.5). Accordingly, for incrementally nonlinear (real) materials, strain bifurcation is possible for *any* hardening/softening modulus $H_c < H \leq H_b$ where the maximum value H_b is determined from the criterion (3.4) for incrementally linear comparison (artificial) solids Benallal and Comi (1996); see (Runesson et al., 1991) for the 2-D case of plane stress and plane strain.

As the hardening/softening modulus H evolves with ongoing inelastic deformations, bifurcation first occurs as a continuous one at a point in the body where conditions are locally favorable. Once the continuous bifurcation is surpassed, deformations and strain concentrate further so that the discontinuous one becomes possible (Rice and Rudnicki, 1980).

Remark 3.1 Regarding rigid-plastic solids, Young's modulus goes to infinity, such that the elastoplastic acoustic tensor cannot be defined. The concept of strain bifurcation does not apply and the bifurcation analysis is unseemly. For isotropic elastoplastic models with associated or non-associated flow rules, Runesson et al. (1991) derived the analytical results for the bifurcation angle and the corresponding hardening/softening modulus H_b in 2-D plane stress and plane strain conditions. It is found that the material under plane stress is more prone to strain localization compared to that under plane strain, and the bifurcation angle in the later case generally depends on Poisson's ratio. Moreover, the occurrence of strain bifurcation depends on the hardening/softening modulus and is thus usually indefinite. Sometimes, multiple solutions exist at a given moment (with the hardening/softening modulus H_b specified *a priori*) as discussed in Ottosen and Runesson (1991). The above facts imply that a more stringent condition is needed to determine the discontinuity band, motivating the strain localization criterion introduced in the next section. □

3.3. Strain localization (SL)

After strain bifurcation occurs, deformations within the discontinuity band become more and more localized, affecting the stress rate (2.8a). Compared to the strain rate $\dot{\boldsymbol{\epsilon}}$ outside the band that is independent of the bandwidth b, the strain rate jump (2.10), inversely proportional to b, is much larger. Consequently, if it were not to cancel out by the third term, the stress rate $\dot{\boldsymbol{\sigma}}$ would become unbounded for a vanishing bandwidth $b \to 0$, which is physically not allowable due to the plastic yielding condition $f(\boldsymbol{\sigma}, q) \leq 0$.

Therefore, additionally to Maxwell's kinematics (2.10) and continuity of the traction rate (2.11), **for the occurrence of strain localization, the stress rate within the discontinuity band has to be independent of the bandwidth whatever the localized strain rate is**.

Remark 3.2 As the strain rate $\dot{\bar{\boldsymbol{\epsilon}}}$ and stress rate $\dot{\bar{\boldsymbol{\sigma}}}$ outside the discontinuity band are always independent of the bandwidth b, the above strain localization condition implies that the stress rate jump $[\![\dot{\boldsymbol{\sigma}}]\!]$ across the band has also to be independent of it. □

Remark 3.3 Regarding strain localization in strain-based elastic-damaging materials, not only the stress rate but also the stress itself have to be independent of the bandwidth; see Wu and Cervera (2017). It is interesting that the

regularized XFEM (Benvenuti et al., 2008; Benvenuti and Orlando, 2021a,b) and the phase-field cohesive zone model (Wu, 2017, 2018a; Wu and Nguyen, 2018; Wu et al., 2020) both concur with the above statement. □

3.3.1. Kinematic conditions

Now let us consider the kinematic conditions upon which the afore-defined strain localization occurs. As the strain rate $\dot{\boldsymbol{\epsilon}}$ outside the discontinuity band does not localize, for the stress rate (2.8a) inside the band to be independent of the bandwidth b, the plastic multiplier $\dot{\lambda} > 0$ has to admit the following additive expression

$$\dot{\lambda} = \dot{\lambda}_0 + \frac{1}{b}\dot{\tilde{\lambda}} \qquad \Longrightarrow \qquad \dot{\boldsymbol{\sigma}} = \mathbb{E}_0 : \left[\dot{\tilde{\boldsymbol{\epsilon}}} - \dot{\lambda}_0 \boldsymbol{\Lambda}^p + \frac{1}{b}\big(\dot{\boldsymbol{w}} \otimes \boldsymbol{n}\big)^{\text{sym}} - \frac{1}{b}\dot{\tilde{\lambda}}\boldsymbol{\Lambda}^p\right] \tag{3.6}$$

where the regular part $\dot{\lambda}_0 \geq 0$ and the localized one $\dot{\tilde{\lambda}} > 0$ are both independent of the discontinuity bandwidth b.

Accordingly, for the stress rate (3.6) to be physically meaningful, the localized terms inversely proportional to the bandwidth b have to cancel out upon strain localization, i.e.,

$$\boxed{\big(\dot{\boldsymbol{w}} \otimes \boldsymbol{n}_s\big)^{\text{sym}} = \dot{\tilde{\lambda}}\boldsymbol{\Lambda}^p} \qquad \Longleftrightarrow \qquad [\![\dot{\boldsymbol{\epsilon}}]\!] = \frac{1}{b}\big(\dot{\boldsymbol{w}} \otimes \boldsymbol{n}_s\big)^{\text{sym}} = \frac{1}{b}\dot{\tilde{\lambda}}\boldsymbol{\Lambda}^p \tag{3.7}$$

That is, **upon strain localization all the strain rate jump, which *is inversely proportional to the bandwidth* b, has to be inelastic (plastic in this work)**. Note that the above kinematic condition depends only on the specific plastic flow tensor $\boldsymbol{\Lambda}^p$ regardless it is associated or non-associated.

Remark 3.4 For rigid-plastic solids, the strain rate within the discontinuity band is purely plastic, such that

$$\dot{\boldsymbol{\epsilon}} = \dot{\tilde{\boldsymbol{\epsilon}}} + \frac{1}{b}\big(\dot{\boldsymbol{w}} \otimes \boldsymbol{n}\big)^{\text{sym}} = \dot{\lambda}\boldsymbol{\Lambda}^p = \dot{\lambda}_0\boldsymbol{\Lambda}^p + \frac{1}{b}\dot{\tilde{\lambda}}\boldsymbol{\Lambda}^p \tag{3.8}$$

where the identity Eq. $(3.6)_1$ has been considered. As the strain rate $\dot{\tilde{\boldsymbol{\epsilon}}}$ does not localize, it follows that

$$\frac{1}{b}\big(\dot{\boldsymbol{w}} \otimes \boldsymbol{n}\big)^{\text{sym}} = \frac{1}{b}\dot{\tilde{\lambda}}\boldsymbol{\Lambda}^p \qquad \Longrightarrow \qquad \big(\dot{\boldsymbol{w}} \otimes \boldsymbol{n}\big)^{\text{sym}} = \dot{\tilde{\lambda}}\boldsymbol{\Lambda}^p \tag{3.9a}$$

as well as

$$\dot{\tilde{\boldsymbol{\epsilon}}} = \dot{\lambda}_0\boldsymbol{\Lambda}^p = \dot{\lambda}_0\dot{\tilde{\lambda}}^{-1}\big(\dot{\boldsymbol{w}} \otimes \boldsymbol{n}\big)^{\text{sym}} \tag{3.9b}$$

where the localized plastic multiplier $\dot{\tilde{\lambda}} > 0$ does not vanish by definition. As can be seen, the strain rate (3.9b) outside the discontinuity is compatible with the assumed rigid behavior, if and only if the following condition is fulfilled

$$\dot{\lambda}_0 = 0 \qquad \Longleftrightarrow \qquad \dot{\tilde{\boldsymbol{\epsilon}}} = \boldsymbol{0} \tag{3.10}$$

That is, in this case strain localization occurs only for the loading/unloading scenarios, which is consistent with the classical result for rigid-plastic solids (Hill, 1950). Note that there is no need to consider the equilibrium equation for strain localization in rigid-plastic solids. □

3.3.2. Stress rate constraints

Upon satisfaction of the strain localization condition (3.7), the stress rate jump (2.9) is independent of the bandwidth b as expected

$$[\![\dot{\boldsymbol{\sigma}}]\!] = \mathbb{E}_0 : \left[\dot{\bar{\lambda}}\bar{\boldsymbol{\Lambda}}^p - \dot{\lambda}_0\dot{\bar{\lambda}}^{-1}\left(\dot{\boldsymbol{w}} \otimes \boldsymbol{n}_s\right)^{\text{sym}}\right] \tag{3.11}$$

Similarly to strain bifurcation, the material points outside the discontinuity band can be in plastic loading or elastic unloading/neutral loading, while those interior points are in plastic loading all along, i.e., $\dot{\bar{\lambda}} > 0$ and $\dot{\bar{\lambda}} \geq 0$. Accordingly, the following two cases are distinguished:

- Loading–loading case (i.e., $\dot{\lambda} > 0$ and $\dot{\bar{\lambda}} > 0$). In this case, the stress rate jump is either null or orthogonal to the normal vector $\boldsymbol{n}_s$, i.e.,

  $$[\![\dot{\boldsymbol{\sigma}}]\!] = \dot{\bar{\alpha}}_{mm}\boldsymbol{m}_s \otimes \boldsymbol{m}_s + \dot{\bar{\alpha}}_{tt}\boldsymbol{t}_s \otimes \boldsymbol{t}_s + \dot{\bar{\alpha}}_{mt}\left(\boldsymbol{m}_s \otimes \boldsymbol{t}_s\right)^{\text{sym}} \tag{3.12}$$

  where the scalars $\dot{\bar{\alpha}}_{mm}$, $\dot{\bar{\alpha}}_{tt}$ and $\dot{\bar{\alpha}}_{mp}$ are all independent of the discontinuity bandwidth b. This is a particular case of Eq. $(2.11)_2$ for strain bifurcation.

- Loading–unloading/neutral loading case (i.e., $\dot{\lambda} > 0$ and $\dot{\bar{\lambda}} = 0$): It then follows that

  $$[\![\dot{\boldsymbol{\sigma}}]\!] = -\dot{\lambda}_0\dot{\bar{\lambda}}^{-1}\mathbb{E}_0 : \left(\dot{\boldsymbol{w}} \otimes \boldsymbol{n}_s\right)^{\text{sym}} \qquad \Longrightarrow \qquad \boldsymbol{n}_s \cdot [\![\dot{\boldsymbol{\sigma}}]\!] = -\dot{\lambda}_0\dot{\bar{\lambda}}^{-1}\boldsymbol{Q}_0 \cdot \dot{\boldsymbol{w}} = \boldsymbol{0} \tag{3.13}$$

  As the elastic acoustic tensor $\boldsymbol{Q}_0 := \boldsymbol{n}_s \cdot \mathbb{E}_0 \cdot \boldsymbol{n}_s$ is symmetric and strictly positive-definite, this condition is fulfilled *if and only if*

  $$\dot{\lambda}_0 = 0 \qquad \Longleftrightarrow \qquad [\![\dot{\boldsymbol{\sigma}}]\!] = \boldsymbol{0} \tag{3.14}$$

  Namely, **in the loading-unloading/neutral loading case, the stress rate is continuous upon strain localization**, even though the stress itselft might be discontinuous due to the accumulation ever since strain bifurcation. This is the case we previously considered for *strain softening solids with associated inelastic laws* (Cervera et al., 2012; Wu and Cervera, 2015, 2016); see Wu and Cervera (2014).

Note that the above condition for strain localization, i.e., independence of the stress rate jump of the bandwidth b, applies to strain discontinuity bands and, in the limit of a vanishing bandwidth b, to strain localization surfaces.

3.3.3. Localization angles: Analytical 2-D results

The strain localization condition (3.7) determines the structure of the flow tensor. More specifically, it implies the existence of a *plastic flow vector* $\boldsymbol{\gamma}$ satisfying (Oliver, 2000; Wu and Cervera, 2015, 2016)

$$\dot{\boldsymbol{w}} = \dot{\bar{\lambda}}\boldsymbol{\gamma} \qquad \Longrightarrow \qquad \boxed{\boldsymbol{\Lambda}^p = \left(\boldsymbol{\gamma} \otimes \boldsymbol{n}_s\right)^{\text{sym}}} \tag{3.15}$$

or in component form of the local axes system (n, m, t) defined at the discontinuity surface $\mathcal{S}$

$$\Lambda^p_{nn} = \gamma_n, \qquad \Lambda^p_{nm} = \frac{1}{2}\gamma_m, \qquad \Lambda^p_{nt} = \frac{1}{2}\gamma_t \tag{3.16a}$$

$$\Lambda^p_{mm} = 0, \qquad \Lambda^p_{tt} = 0, \qquad \Lambda^p_{mt} = 0 \tag{3.16b}$$

From the kinematic constraint (3.15) or (3.16), the orientation of the discontinuity surface can be determined.

Regarding the 2-D case of plane stress and plane strain, the localization angle θ_ℓ can be determined from the condition (3.16b). Interestingly, our previous analytical results for isotropic (Wu and Cervera, 2014, 2015, 2016) and orthotropic (Cervera et al., 2020) plasticity with associated evolution laws also applies to the non-associated case. Here these results are summarized for the sake of later validations.

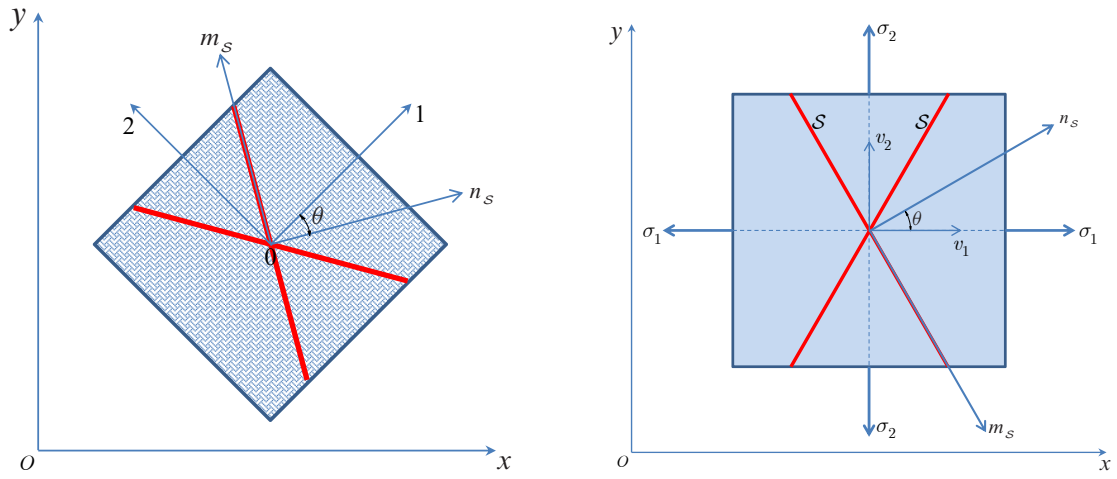

(a) Orthotropic plastic solids

(b) Isotropic plastic solids

Figure 3: Definitions of the discontinuity angle θ in isotropic and orthotropic plastic solids

- Orthotropic plasticity. As shown in Figure 3(a), let us consider the problem in the material axes $(1, 2, 3)$. The orientation of the discontinuity band is characterized by the inclination angle (counter-clockwise) $\theta_\ell \in [-\pi/2, \pi/2]$ between the normal vector $\boldsymbol{n}_S$ and the material axis 1.

  In this case, the condition $(3.16b)_2$ gives (Cervera et al., 2020)

$$\tan\theta_\ell = -\frac{\Lambda^p_{12}}{\Lambda^p_{11}} \pm \sqrt{\left(\frac{\Lambda^p_{12}}{\Lambda^p_{11}}\right)^2 - \frac{\Lambda^p_{22}}{\Lambda^p_{11}}} \tag{3.17}$$

  As can be seen, the discontinuity angle θ_ℓ depends on the stress state upon strain localization.

- Isotropic plasticity. In this case, it is more convenient to define the discontinuity angles in the principal axes of the flow tensor $\boldsymbol{\Lambda}^p$ (coincident with those of the stress tensor $\boldsymbol{\sigma}$) as shown in Figure 3(b). The in-plane components along these principal axes are defined as $(\Lambda^p_1, \Lambda^p_2)$, while Λ^p_3 are associated with the out-of-plane

principal direction. The discontinuity angle (counter-clockwise) $\theta_\ell \in [-\pi/2, \pi/2]$ between the normal vector $\boldsymbol{n}_{\mathcal{S}}$ and the principal vector $\boldsymbol{v}_1$ of the stress tensor $\boldsymbol{\sigma}$ is determined by (Wu and Cervera, 2015, 2016)

$$\tan\theta_\ell = \pm\sqrt{-\frac{\Lambda_2^p}{\Lambda_1^p}} \tag{3.18}$$

which corresponds exactly to the case of $\Lambda_{12}^p = 0$ for the orthotropic result (3.17). Here axes are labeled so that $\Lambda_1^p \geq \Lambda_2^p$, and the magnitude of the out-of-plane components Λ_3^p is not related directly to the magnitude of those in-plane.

For the plane stress case, Eq. (3.16b)$_2$ is automatically satisfied and thus Eq. (3.17) or Eq. (3.18) alone determines the localization angle θ_ℓ. Contrariwise, in the plane strain condition, the localization angle given by Eq. (3.17) or Eq. (3.18) is further constrained by the out-of-plane stress σ_3 that satisfies (Wu and Cervera, 2016)

$$\Lambda_{33}^p(\theta_\ell) = 0 \tag{3.19}$$

upon strain localization.

Remark 3.5 The out-of-plane stress satisfying (3.19) is in general different from the elastic value

$$\sigma_3 = \nu_0(\sigma_1 + \sigma_2) \tag{3.20}$$

Therefore, in the case of plane strain, except for very particular cases, strain localization does not occur at the onset of plastic yielding. Rather, substantial plastic flows have to occur after plastic yielding (and possibly, strain bifurcation), until the out-of-plane stress fulfills Eq. (3.19). □

Remark 3.6 As the localization angle θ_ℓ is not affected by the elastic constants like Young's modulus and Poisson's ratio, the above results also apply to orthotropic elasticity. □

3.4. Discussion

From the above analyses, the following comments can be made:

(1) For both strain bifurcation and localization, the strain (rate) field exhibits discontinuities and the corresponding jump across the discontinuity band is given by Maxwell's kinematics. Moreover, the material inside the band is in plastic loading, but the one outside it can be either in plastic/neutral loading or elastic unloading.

(2) For both strain bifurcation and localization, continuity of the traction rate implies that stress rate discontinuities can take place only on the plane parallel to the discontinuity surface.

(3) Strain bifurcation is only a necessary condition for strain localization, while the latter is more demanding with the extra condition that the stress rate within the discontinuity band has to be independent of the bandwidth.

(4) In the plane strain condition there is a transition stage between plastic yielding (and possibly, strain bifurcation) and strain localization. During this stage the stress rate within the discontinuity band may depend on the bandwidth.

(5) The occurrence of strain localization depends only on the plastic potential function, regardless of the flow rule is associated or non-associated. It depends neither on the plastic yield function (provided it is activated) nor on the elastic constants like Poisson's ratio as that for strain bifurcation.

4. The mechanics of strain localization: Discrete setting

In this section the above strain localization condition and the analytical results for the discontinuity angles presented in 3.3.3 are numerically verified by finite element simulations. In particular, full boundary value problems (BVPs) are set up, discretized and solved, completed with the corresponding boundary conditions and increasing applied loading. Consequently, the obtained solutions have spatial variation and time evolution. Also, they are subjected to approximation errors (discretization in space and time, nonlinear tolerances, etc). Therefore, the comparison of the analytical results to the discrete solutions has to be interpreted on this regard.

In the numerical simulations, the plastic potential functions of the von Mises and the Hill criteria are considered, both being pressure independent and producing perfectly isochorich plastic flow by definition. Accordingly, for the occurrence of strain localization the plastic flow needs to be well developed and, at that stage, the incompressible plastic deformation is dominant over the elastic one. Standard displacement-based finite elements are not well suited to cope with this quasi-incompressibility situation in particular, if low-order finite elements are used. Mixed displacement/pressure ($\mathbf{u}/p$) finite elements are far more suitable (Simó and Hughes, 1998); see our previous works on this topic (Chiumenti et al., 2002, 2004; Cervera et al., 2003b,a, 2004; Cervera and Chiumenti, 2009; Cervera et al., 2012).

4.1. The stabilized mixed $\boldsymbol{u}/p$ formulation

The strong form of the mixed $\boldsymbol{u}/p$ formulation for mechanical problems is stated as: Given the elastic properties (G_0, K_0) and prescribed body forces $\boldsymbol{b}^*$, find the displacement $\boldsymbol{u}$ and pressure p, such that

$$\begin{cases} \nabla \cdot \boldsymbol{s} + \nabla p + \boldsymbol{b}^* = \boldsymbol{0} \\ \nabla \cdot \boldsymbol{u} - \dfrac{1}{K_0} p = 0 \end{cases} \tag{4.1}$$

where $\boldsymbol{s} = 2G_0\big(\boldsymbol{e} - \boldsymbol{e}^p\big)$ is the deviatoric stress tensor, with $\boldsymbol{e}$ and $\boldsymbol{e}^p$ being the deviatoric strain tensor and its plastic component; G_0 and K_0 denote the shear and bulk moduli, respectively.

Standard arguments yield the following discrete form

$$\begin{cases} \displaystyle\int_\Omega \nabla^{\text{sym}} \delta\boldsymbol{u}_h : \boldsymbol{s}_h \, \mathrm{d}V + \int_\Omega \big(\nabla \cdot \delta\boldsymbol{u}_h\big) p_h \, \mathrm{d}V = \int_\Omega \delta\boldsymbol{u}_h \cdot \boldsymbol{b}^* \, \mathrm{d}V + \int_{\partial\Omega_t} \delta\boldsymbol{u}_h \cdot \boldsymbol{t}^* \, \mathrm{d}A & \forall \delta\boldsymbol{u}_h \\ \displaystyle\int_\Omega \delta p_h \, \big(\nabla \cdot \boldsymbol{u}_h\big) - \int_\Omega \delta p_h \frac{1}{K_0} p_h \, \mathrm{d}V = 0 & \forall \delta p_h \end{cases} \tag{4.2}$$

where $(\boldsymbol{u}_h, p_h)$ and $(\delta\boldsymbol{u}_h, \delta p_h) \in \mathscr{V}_h \times \mathscr{Q}_h$ denote the discrete displacement and pressure fields and their variations.

In mixed formulations, it is challenging to construct appropriate interpolating finite element spaces that satisfy the stability requirements on the spaces $\mathscr{V}_h$ and $\mathscr{Q}_h$ (Brezzi and Fortin, 1991). For instance, standard mixed elements

with continuous equal-order linear/linear interpolation for both fields are not stable. Fortunately, stabilization methods (Hughes, 1995; Hughes et al., 1998) can be developed to attain global stability with the desired choice of interpolation spaces. An appealing stabilization method is the orthogonal sub-grid scale method (Codina and Blasco, 1997; Codina, 2000), previously applied to the problem of incompressible elasto-plasticity (Chiumenti et al., 2002, 2004; Cervera et al., 2003b,a, 2004; Cervera and Chiumenti, 2009; Cervera et al., 2012).

The basic idea of the orthogonal sub-grid scale approach is to split the continuous displacement field into a coarse scale component and a fine one, corresponding to different scales or levels of resolution, i.e.,

$$\boldsymbol{u} = \boldsymbol{u}_h + \boldsymbol{u}_\perp \tag{4.3}$$

where $\boldsymbol{u}_h \in \mathscr{V}_h$ is the displacement field of the (coarse) finite element scale; $\boldsymbol{u}_\perp$ is the enriched displacement field corresponding to the fine sub-grid scale, located in the space orthogonal to the finite element space and given by

$$\boldsymbol{u}_\perp = \tau_e\big(\boldsymbol{r}_h - P_h(\boldsymbol{r}_h)\big) \qquad \text{with} \qquad \boldsymbol{r}_h = \nabla\cdot\boldsymbol{s}_h + \nabla p_h + \boldsymbol{b}^* \tag{4.4}$$

for the L_2-projection P_h onto $\mathscr{V}_h$. Here, the stabilization parameter is determined by $\tau_e = ch_e^2/(2G_0)$ with h_e being the characteristic length of the element and $c = \mathcal{O}(1)$ being a constant. As the stabilization (4.4) is residual-based, it is consistent; that is, it converges upon mesh refinement and vanishes for the continuous solution. The mesh size dependent stabilization parameter adopted achieves optimal convergence rate (Codina and Blasco, 1997; Codina, 2000).

Accordingly, the resulting stabilized mixed system of equations is expressed as

$$\begin{cases} \displaystyle\int_\Omega \nabla^{\text{sym}}\delta\boldsymbol{u}_h : \boldsymbol{s}_h \,\mathrm{d}V + \int_\Omega \big(\nabla\cdot\delta\boldsymbol{u}_h\big) p_h \,\mathrm{d}V = \int_\Omega \delta\boldsymbol{u}_h\cdot\boldsymbol{b}^* \,\mathrm{d}V + \int_{\partial\Omega_t} \delta\boldsymbol{u}_h\cdot\boldsymbol{t}^* \,\mathrm{d}A & \forall\delta\boldsymbol{u}_h \\ \displaystyle\int_\Omega \delta p_h \,\big(\nabla\cdot\boldsymbol{u}_h\big) - \int_\Omega \delta p_h \frac{1}{K_0} p_h \,\mathrm{d}V - \int_\Omega \delta p_h \tau_e\big(\nabla p_h - \pi_h\big) \,\mathrm{d}V = 0 & \forall\delta p_h \end{cases} \tag{4.5}$$

where the nodal variable $\pi_h = P_h(\nabla p_h)$ is the L_2-projection of the pressure gradient.

4.2. Benchmark verification

The above mixed stabilized $\boldsymbol{u}/p$ element is then applied to the strain localization analysis. The benchmark example is a 2-D strip loaded in uniaxial tension by stretching via imposed vertical displacements at the top and bottom ends; horizontal movement is not restrained. Figure 4(a) depicts the geometry of the problem with dimensions 10 m $\times$ 20 m $\times$1 m (width $\times$ height $\times$ thickness). A sharp horizontal slit of length 2 m is inserted in the strip to introduce the perturbation necessary to trigger strain localization. As the plane stress condition has been previously numerically studied in Cervera et al. (2012) for isotropic plasticity and in Cervera et al. (2020) for orthotropic one, only the plane strain condition is considered in this work. The remote stress state corresponds to

$$\sigma_{xx} = 0, \qquad \sigma_{yy} = \sigma, \qquad \sigma_{xy} = 0 \tag{4.6}$$

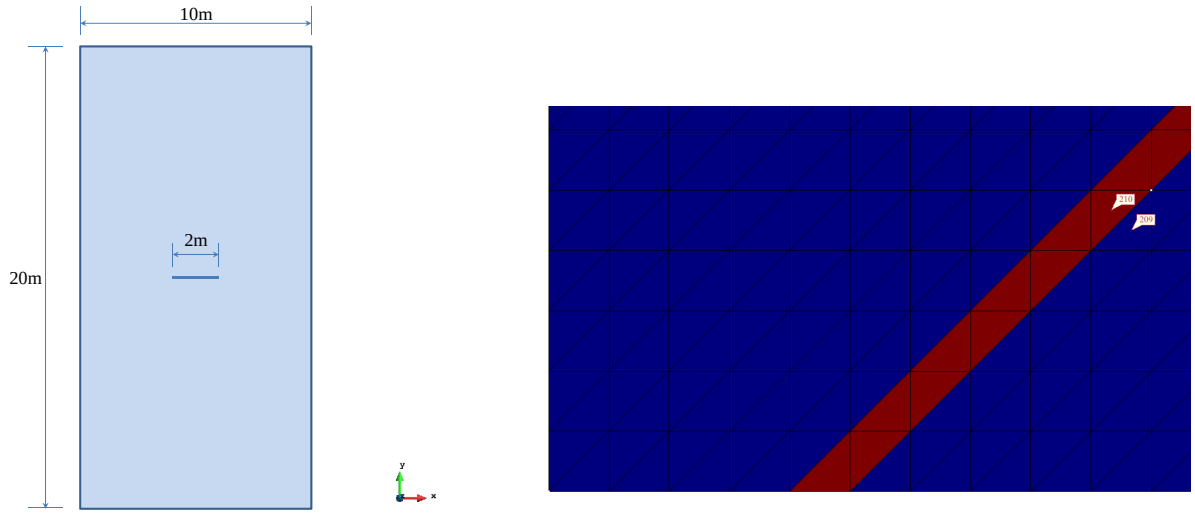

(a) Geometry (b) Finite element mesh and material points inside and outside the discontinuity band

Figure 4: A plane strain strip under vertical stretching: Dimensions and finite element mesh. The bottom and top edges are vertically stretched along opposite directions but with equal magnitude. The flags in (b) indicate the actual elements inside and outside the localization band where the variables in Figures 7, 9, 11 and 13 are sampled.

The numerical results are then used to validate the proposed strain localization criterion and verify the analytical results for the discontinuity orientation.

Several elastoplastic models, i.e., the isotropic von Mises model and the orthotropic Hill model with associated flow rules, and the von Mises model with the non-associated Hill evolution law, all being isochoric, are considered for the material. Without loss of generality, the yield function is of the following form

$$f(\boldsymbol{\sigma}, q) := \phi(\boldsymbol{\sigma}) - q \leq 0 \tag{4.7}$$

for the loading function $\phi(\boldsymbol{\sigma})$ and the yield strength q

$$\phi(\boldsymbol{\sigma}) = \sqrt{\frac{3}{2}\boldsymbol{\sigma}^{\mathrm{T}}\,\mathbf{P}\,\boldsymbol{\sigma}}, \qquad q = \frac{3}{2}\big(F+G+H\big)^{-1} \tag{4.8}$$

where $\boldsymbol{\sigma} := \big\{\sigma_{11}, \sigma_{22}, \sigma_{33}, \sigma_{12}, \sigma_{13}, \sigma_{23}\big\}^{\mathrm{T}}$ represents the stress vector in the Voigt notation, with $\sigma_{11}, \sigma_{22}, \sigma_{33}, \sigma_{12}, \sigma_{13}$ and σ_{23} denoting the stress components in the material axes $(1, 2, 3)$. Regarding the orthotropic Hill model, the projection matrix $\mathbf{P}$ is given by

$$\mathbf{P} = \frac{1}{F+G+H}\begin{bmatrix} F+G & -F & -G & 0 & 0 & 0 \\ -F & F+H & -H & 0 & 0 & 0 \\ -G & -H & G+H & 0 & 0 & 0 \\ 0 & 0 & 0 & 2L & 0 & 0 \\ 0 & 0 & 0 & 0 & 2M & 0 \\ 0 & 0 & 0 & 0 & 0 & 2N \end{bmatrix} \tag{4.9}$$

for the following material parameters F, G, H, L, M and N

$$F = \frac{1}{2}\left[\left(\frac{1}{\sigma_{Y,11}}\right)^2 + \left(\frac{1}{\sigma_{Y,22}}\right)^2 - \left(\frac{1}{\sigma_{Y,33}}\right)^2\right], \qquad L = \frac{1}{2}\left(\frac{1}{\sigma_{Y,12}}\right)^2 \tag{4.10a}$$

$$G = \frac{1}{2}\left[\left(\frac{1}{\sigma_{Y,11}}\right)^2 + \left(\frac{1}{\sigma_{Y,33}}\right)^2 - \left(\frac{1}{\sigma_{Y,22}}\right)^2\right], \qquad M = \frac{1}{2}\left(\frac{1}{\sigma_{Y,13}}\right)^2 \tag{4.10b}$$

$$H = \frac{1}{2}\left[\left(\frac{1}{\sigma_{Y,22}}\right)^2 + \left(\frac{1}{\sigma_{Y,33}}\right)^2 - \left(\frac{1}{\sigma_{Y,11}}\right)^2\right], \qquad N = \frac{1}{2}\left(\frac{1}{\sigma_{Y,23}}\right)^2 \tag{4.10c}$$

where those entities embellished by subscripts "Y" representing the corresponding yield strengths. The isotropic von Mises model is recovered with $\sigma_{Y,11} = \sigma_{Y,22} = \sigma_{Y,33} = \sqrt{3}\sigma_{Y,12} = \sqrt{3}\sigma_{Y,13} = \sqrt{3}\sigma_{Y,23} = \sigma_Y$ and $q = \sigma_Y$.

The following material properties are assumed in the numerical simulations: Young's modulus $E_0 = 10$ MPa, the yield strength $\sigma_Y = 10$ KPa for isotropic plastic models and $\sigma_{Y,11} = 15$ KPa with all the others equal to 10 kPa for orthotropic ones (no tilt is considered such that the material axes coincide with the global ones). It then follows that

$$\begin{cases} F = G = H = \frac{1}{2}\left(\frac{1}{\sigma_Y}\right)^2, \quad M = N = L = \frac{3}{2}\left(\frac{1}{\sigma_Y}\right)^2 & \text{the von Mises yield function} \\ F = G = \frac{2}{9}\left(\frac{1}{\sigma_Y}\right)^2, \quad H = \frac{7}{9}\left(\frac{1}{\sigma_Y}\right)^2, \quad L = M = N = \frac{3}{2}\left(\frac{1}{\sigma_Y}\right)^2 & \text{the Hill yield function} \end{cases} \tag{4.11}$$

The double symmetry of the problem and the solution allows to discretize a quarter of the domain. Various Poisson's ratio ν_0 are discussed for comparison purposes.

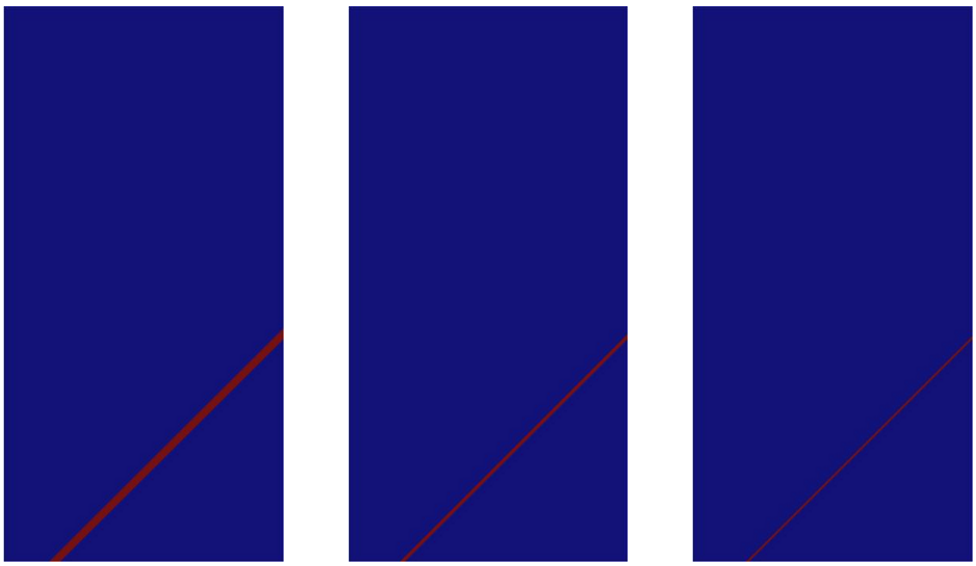

(a) Mesh M1 (b) Mesh M2 (c) Mesh M3

Figure 5: Localization angles for the finite element meshes with various sizes.

As the identity $\Lambda^p_{12} = 0$ holds for the von Mises potential function and the Hill one with no tilt, it follows from Eq. (4.16) that the localization angles are both $\theta_\ell = 45°$; see Remark 4.1. Accordingly, structured triangular meshes

are used in all the simulations to optimize the capacity of the linear triangles to represent a pure sliding mode, in parallel to one of the element sides; see Figure 4(b). In each example, three meshes of various sizes, i.e., $h_e = 0.02$ m, 0.01 m and 0.005 m, are considered. As can been shown in Figure 5, for all cases the deformations are localized into narrow discontinuity bands of one single row of elements along $\pm 45°$ directions, with the bandwidth proportional to the mesh size, i.e., $b = \sqrt{2}\, h_e$.

Calculations are performed with an enhanced version of the finite element program COMET (Cervera et al., 2002), developed by the authors at the International Center for Numerical Methods in Engineering (CIMNE). Pre- and post-processing is done with GiD, also developed at CIMNE (CIMNE, 2009). Loading is applied by imposed vertical displacements at both ends of the strip. The Newton–Raphson method is used to solve the nonlinear system of equations arising from the spatial and temporal discretization of the problem. An automatic procedure is used to adjust the step size, and about 200 steps are necessary to complete the analyses. Convergence of a time step is attained when the ratio between the norms of the residual and the total forces is smaller than 10^{-3}.

The purpose of these benchmark examples is two-fold: *(i)* to validate the proposed strain localization condition by comparing the mesh size (or, equivalently, bandwidth) independence of the stress (rate) inside the discontinuity band, and *(ii)* to identify plastic yielding (PY), strain bifurcation (SB) and strain localization (SL) by monitoring stress and strain evolution of two neighboring points inside and right outside of the discontinuity band (see the flags in Figure 4(b)):

- Plastic yielding (PY): PY is identified as the linear elastic limit of the stress – strain curves of the material point inside the discontinuity band. It can be determined by the change of slope observed in the evolution of the stresses and the Lode angle as plastic strains start to develop. For the current stress state and material parameters, it occurs when the vertical stress reaches

$$\sigma_{yy} = \begin{cases} \dfrac{\sigma_Y}{\sqrt{1-\nu_0+\nu_0^2}} & \text{the von Mises yield function} \\ \dfrac{\sigma_Y}{\sqrt{1-\frac{14}{9}\nu_0+\nu_0^2}} & \text{the Hill yield function} \end{cases} \tag{4.12}$$

- Strain bifurcation (SB): SB is identified by definition as the moment right after the curves of the strain components of the material points inside and outside the discontinuity band start deviating. However, as the corresponding strains are small, the onset of strain bifurcation is not always easy to determine by inspection: it comes soon after plastic yielding and it triggers the transition phase into strain localization.

  Regarding the current example involving perfectly plasticity, SB is identified as the moment when the discontinuity band is passing through the material point, manifested by a local peak of the stress curves. After that, rotation of the discontinuity orientation occurs until the SL condition is activated.

- Strain localization (SL): SL is identified as the moment upon which the Lode angle corresponding to the strain localization condition $\Lambda^p_{33}(\theta_\ell) = 0$ is fulfilled at the material point inside the discontinuity band. This is

feasible because plastic flow depends only on the deviatoric stresses and the strain localization condition is determined also by the corresponding Lode angle $\tilde{\theta}$. More specifically, for the von Mises and Hill potential functions, the out-of-plane stress σ_3 fulfilling the condition (3.19) is given by

$$\sigma_3 = \begin{cases} \dfrac{1}{2}\sigma & \text{the von Mises potential function} \\ \dfrac{7}{9}\sigma & \text{the Hill potential function} \end{cases} \tag{4.13}$$

Regarding the stress state (4.6) and (4.13), the Lode angle (positive cosine) $\tilde{\theta} \in [0, \pi/3]$ is determined as

$$\tilde{\theta} = \frac{1}{3}\arccos\left[\frac{J_3}{2}\left(\frac{3}{J_2}\right)^{3/2}\right] = \begin{cases} 30^\circ & \text{the von Mises potential function} \\ 47.78^\circ & \text{the Hill potential function} \end{cases} \tag{4.14}$$

where J_2 and J_3 denote the second and third invariants of the deviatoric stress tensor $\boldsymbol{s}$.

Perfect plasticity is considered in Section 4.2.1 $\sim$ Section 4.2.4, while the results presented in Section 4.2.5 indicate that the proposed strain localization condition also applies to softening plasticity (Wu and Cervera, 2016).

Remark 4.1 For the plastic models with Eqs. (4.8)$\sim$(4.10) being the potential functions, in the plane strain cases ($\epsilon_3 = 0$) the condition (3.19) gives the following out-of-plane stress

$$\sigma_{33} = \frac{G\sigma_{11} + H\sigma_{22}}{G + H}, \qquad \Lambda^p_{11} + \Lambda^p_{22} = -\Lambda^p_{33} = 0 \tag{4.15}$$

Accordingly, Eq. (3.17) becomes

$$\tan\theta_\ell = -\frac{\Lambda^p_{12}}{\Lambda^p_{11}} \pm \sqrt{\left(\frac{\Lambda^p_{12}}{\Lambda^p_{11}}\right)^2 + 1} \tag{4.16}$$

for the ratio

$$\frac{\Lambda^p_{12}}{\Lambda^p_{11}} = \frac{(G+H)L}{FG + FH + GH} \cdot \frac{\sigma_{12}}{\sigma_{11} - \sigma_{22}} \tag{4.17}$$

It follows from Eq. (4.16) that

$$\tan\theta_{\ell 1} \cdot \tan\theta_{\ell 2} = -1 \qquad \Longrightarrow \qquad \left|\theta_{\ell 1} - \theta_{\ell 2}\right| = 90^\circ \tag{4.18}$$

Accordingly, in the plane strain condition the discontinuity bands are perpendicular to each other. For the particular case of isotropic von Misese model, it follows from $\Lambda^p_{12} = 0$ that $\theta_\ell = \pm 45^\circ$. □

4.2.1. The associated von Mises model with Poisson's ratio $\nu_0 = 0.0$

Let us first consider the associated von Mises model with Poisson's ratio $\nu_0 = 0.0$. For the material point within the discontinuity band, the evolution curves of the vertical strain, the vertical and out-of-plane stresses, and the Lode angle given by various mesh sizes are shown in Figure 6.

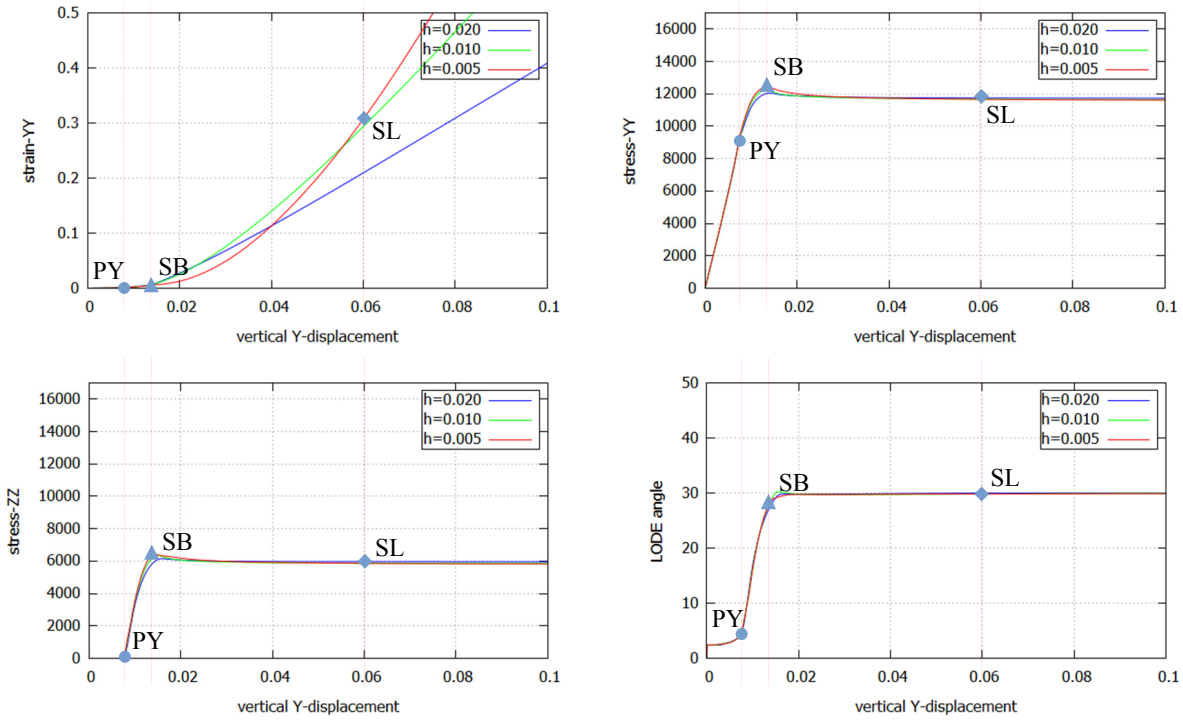

Figure 6: Strain, stresses and Lode angle of the von Mises model with Poisson's ratio $\nu_0 = \mathbf{0.0}$: Effect of the bandwidth (mesh size)

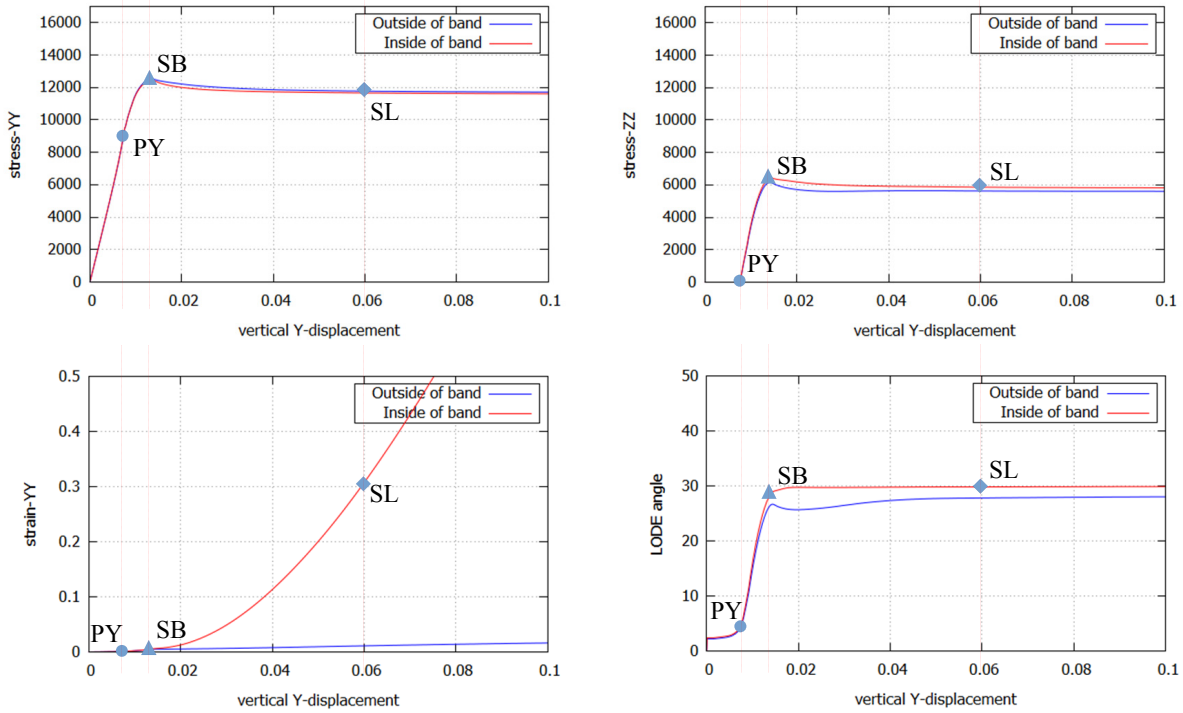

Figure 7: Evolution curves of the von Mises model with Poisson's ratio $\nu_0 = \mathbf{0.0}$.

As expected, the vertical strain ϵ_{yy} depends on the discontinuity bandwidth (or, equivalently, the mesh size): the less the bandwidth b is, the larger strain it reaches. Moreover, except during the intermediate transition stage, the stress components σ_{yy} and σ_{zz}, and the Lode angle $\tilde{\theta}$, are all independent of the bandwidth b, validating the assumption postulated before: for the occurrence of strain localization, the stress rate inside the discontinuity band is independent from the mesh size and the resulting discontinuity bandwidth. Accordingly, termination of the transition stage can be identified as the strain localization point.

In order to identify plastic yielding (PY), strain bifurcation (SB) and strain localization (SL), the evolution curves of stress and strain at two neighboring points inside and right outside of the discontinuity band are considered in Figure 7. Here only the results given by the mesh size $h_e = 0.005$ m are presented. In Figure 7(a) the evolution curves of the stress σ_{yy} is shown. Plastic yielding is identified as the loss of linearity. For this case of vanishing Poisson's ratio $\nu_0 = 0.0$, another signal of plastic yielding is the occurrence of non-vanishing out-of-plane stress σ_{zz} as depicted in Figure 7(b).

The evolution curves of the strain ϵ_{yy} are depicted in Figure 7(c). Though strain bifurcation is defined as the deviation of the strains inside and outside of the band, it corresponds to the peak points of the stress curves. The evolution curves of Lode angle $\tilde{\theta}$ are shown in Figure 7(d). Strain localization is identified as the moment upon which the Lode angle $\tilde{\theta} = 30°$ for the material point inside the discontinuity band. Compared to strain bifurcation, strain localization occurs much later and there is a transition stage between them allowing the out-of-plane stress (3.19) to be attained.

As can be seen from the evolution curves of σ_{yy} and σ_{zz}, upon strain bifurcation the stresses inside and outside the discontinuity band start deviating from each other. This stress jump that evolves during the transition phase from strain bifurcation to straing localization, remains constant, i.e., $[\![\dot{\boldsymbol{\sigma}}]\!] = \boldsymbol{0}$, after strain localization, validating the stress rate continuity condition (3.14). This is because the material point outside the discontinuity band is in neutral loading.

4.2.2. The associated von Mises model with Poisson's ratio $\nu_0 = 0.5$

Let us next consider the associated von Mises model with Poisson's ratio $\nu_0 = 0.5$. As shown in Figure 8, except for the vertical strain ϵ_{yy}, the vertical and lateral stresses $(\sigma_{yy}, \sigma_{zz})$ as well as the Lode angle $\tilde{\theta}$ are all independent of the discontinuity bandwith b almost during the whole deformation process. The observed very minor deviations are caused by stress perturbations during the formation of the discontinuity band and its passing through the sampling point.

As shown in Figure 9 , in this case plastic yielding (PY), strain bifurcation (SB) and strain localization (SL) are very close to each other. This is because the out-of-plane stress (3.19) for $\nu_0 = 0.5$ is coincident with the elastic value (3.20) and no transition stage exists. The minor differences in-between them is caused by the crossing of the discontinuity band through the material point. As there is no transition stage allowing stress discontinuities to develop, the stresses are continuous across the discontinuity band and the stress continuity holds together with the stress rate continuity, i.e., $[\![\boldsymbol{\sigma}]\!] = [\![\dot{\boldsymbol{\sigma}}]\!] = \boldsymbol{0}$.

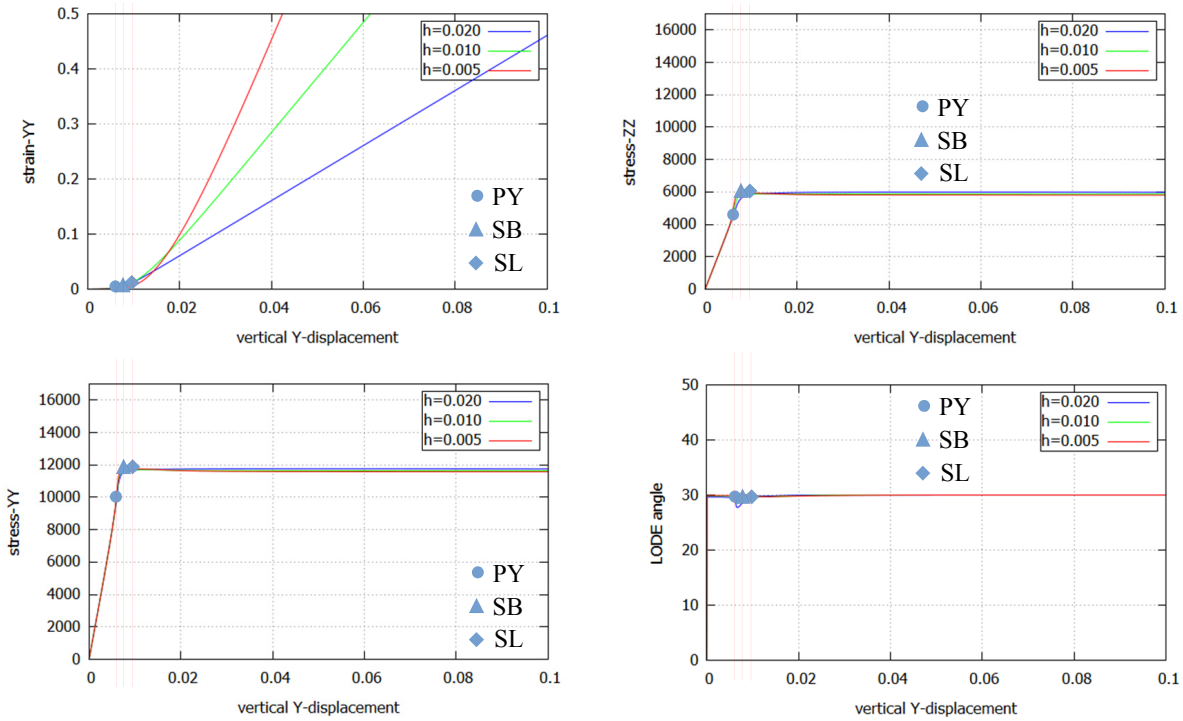

Figure 8: Strain, stresses and Lode angle of the von Mises model with Poisson's ratio $\nu_0 = 0.5$: Effect of the bandwidth (mesh size)

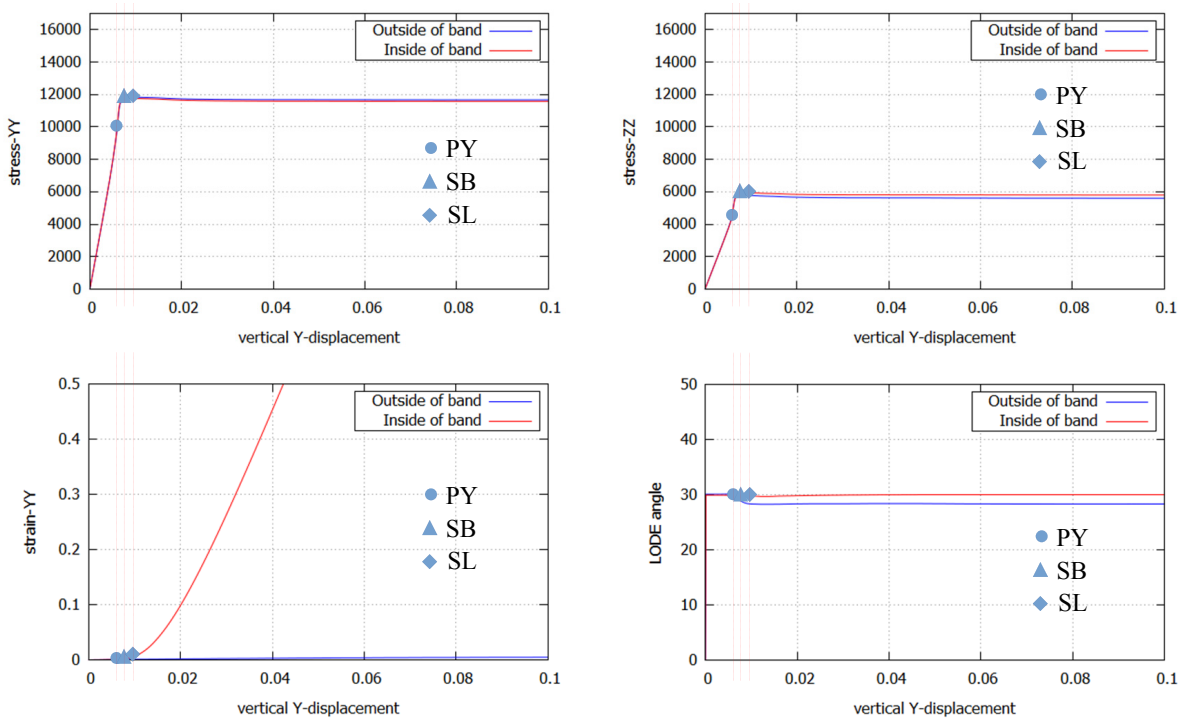

Figure 9: Evolution curves of the von Mises model with Poisson's ratio $\nu_0 = 0.5$.

4.2.3. The associated Hill model with Poisson's ratio $\nu_0 = 0.2$

Next the associated Hill model with Poisson's ratio $\nu_0 = 0.2$ is considered. Again, Figure 10 confirms that the strain field inside the discontinuity band is dependent of the bandwidth b as expected, but the non-vanishing stress components σ_{yy} and σ_{zz} as well as the Lode angle $\tilde{\theta}$ are all independent of it except during the intermediate transition stage between strain bifurcation and localization.

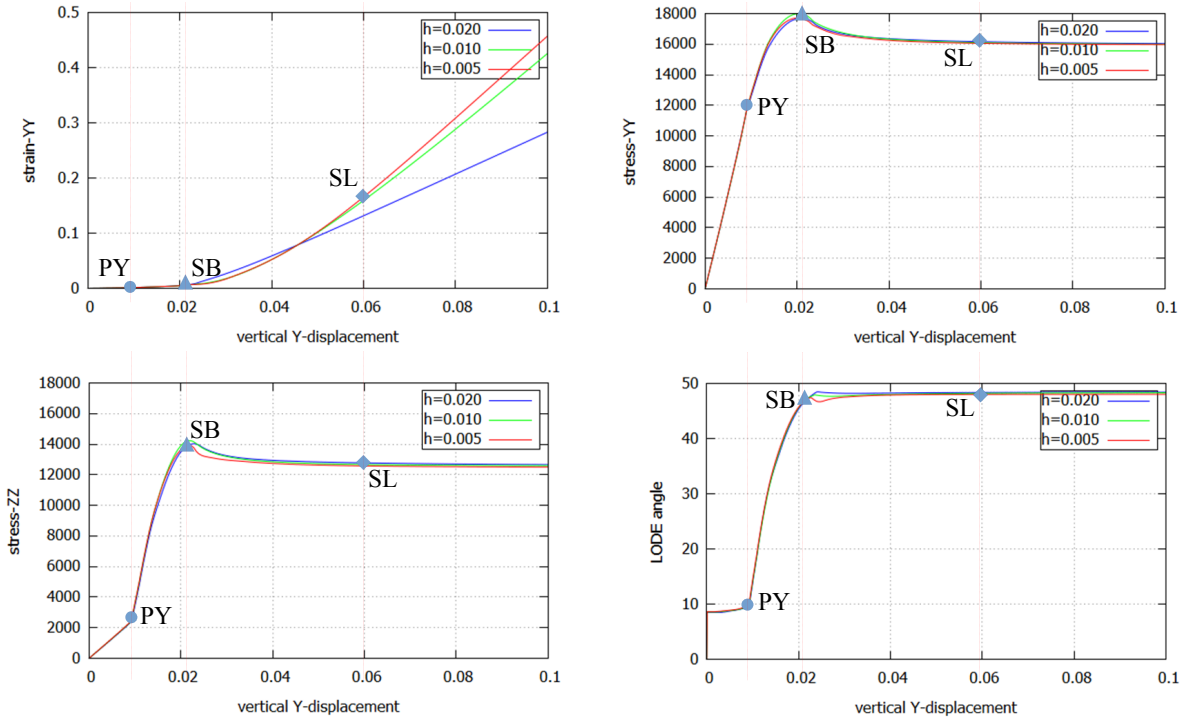

Figure 10: Strain, stresses and Lode angle of the associated Hill model with Poisson's ratio $\nu_0 = 0.2$: Effect of the bandwidth (mesh size)

In this case, plastic yielding (PY) and strain bifurcation (SB), which are identified from the evolution curves of σ_{yy} and σ_{zz} shown in the Figure 11(a, b) as the loss of linearity of these curves and from Figure 11(c, d) as the deviation of the strains inside and outside the discontinuity band, respectively. The latter is more easily identified as the peak points of the stress curves. As the out-of-plane stress $(4.13)_2$ cannot be attained at the onset of plastic yielding, there is a transition stage until the plane strain localization occurs with a Lode angle $\tilde{\theta} = 47.78°$; see Figure 11(d).

Moreover, though the gaps between the stresses inside and outside the discontinuity band vary during the transition stage, the stress rate continuity condition $[\![\dot{\boldsymbol{\sigma}}]\!] = \boldsymbol{0}$ holds upon strain localization (SL) and thereafter. That is, the postulated assumption of stress (rate) objectivity upon strain localization also applies to orthotropic plastic solids.

4.2.4. The non-associated von Mises/Hill model with Poisson's ratio 0.2

Finally, let us consider the non-associated plastic model with the von Mises yield function and the Hill potential function. Poisson's ratio $\nu_0 = 0.2$ is assumed. Figure 12 depicts the evolution curves of the vertical strain, the non-

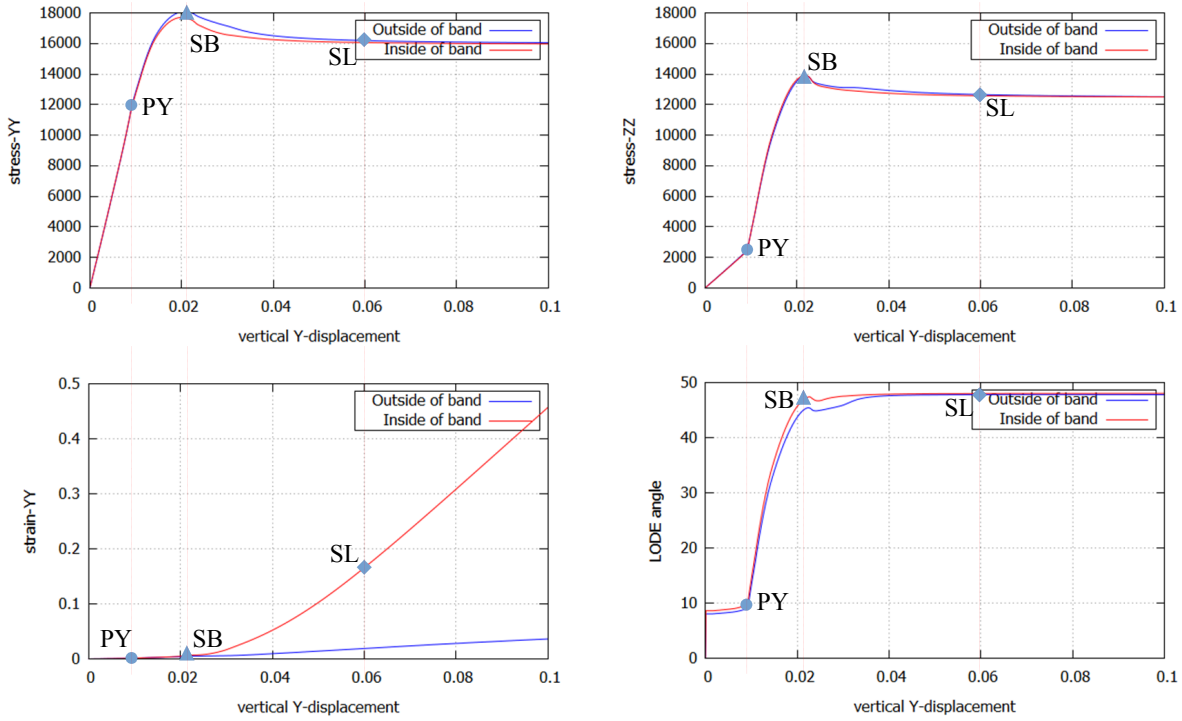

Figure 11: Evolution curves of the Hill model with Poisson's ratio $\nu_0 = 0.2$.

vanishing stresses and the Lode angle inside the discontinuity band. As can be seen, for this non-associated plastic solid the stresses are also independent of the bandwidth upon strain localization and thereafter, though the strain becomes larger as the mesh size decreases.

Plastic yielding and strain bifurcation are easily identified from the loss of linearity and the peak load of the stress curves shown in Figure 13(a). Similarly, as the out-of-plane stress $(4.13)_2$ upon strain localization is not equal to the elastic one upon plastic yielding and strain bifurcation, a transition stage presents in Figure 13(d) during which substantial deviatoric plastic flow occurs until the stress state inside the band corresponds to a Lode angle $\tilde{\theta} = 47.78°$. Again, as can be seen from the evolution curves of σ_{yy} and σ_{zz}, upon strain localization the stress discontinuities inside and outside the band stop increasing and the stress gaps maintain constant, i.e., $[\![\dot{\boldsymbol{\sigma}}]\!] = \boldsymbol{0}$.

4.2.5. Localization in softening plasticity

In this subsection, the four cases studied in the preceding subsections for perfect plasticity are computationally re-analyzed for softening plasticity. For each case, three meshes of various sizes, i.e., $h_e = 0.02$ m, 0.01 m and 0.005 m, respectively, are considered as in the case of perfect plasticity. Exponential softening is considered for the yield-stress q in Eq. (4.7). Dissipation is controlled by relating the softening parameters to the fracture energy (Wu and Cervera, 2016) and the mesh size, though other strategies can be used as well (Poh and Swaddiwudhipong, 2009; Martínez-Pañeda and Betegón, 2015). A fracture energy $G_{\mathrm{f}} = 1,250$ J/m^2 is used in all cases.

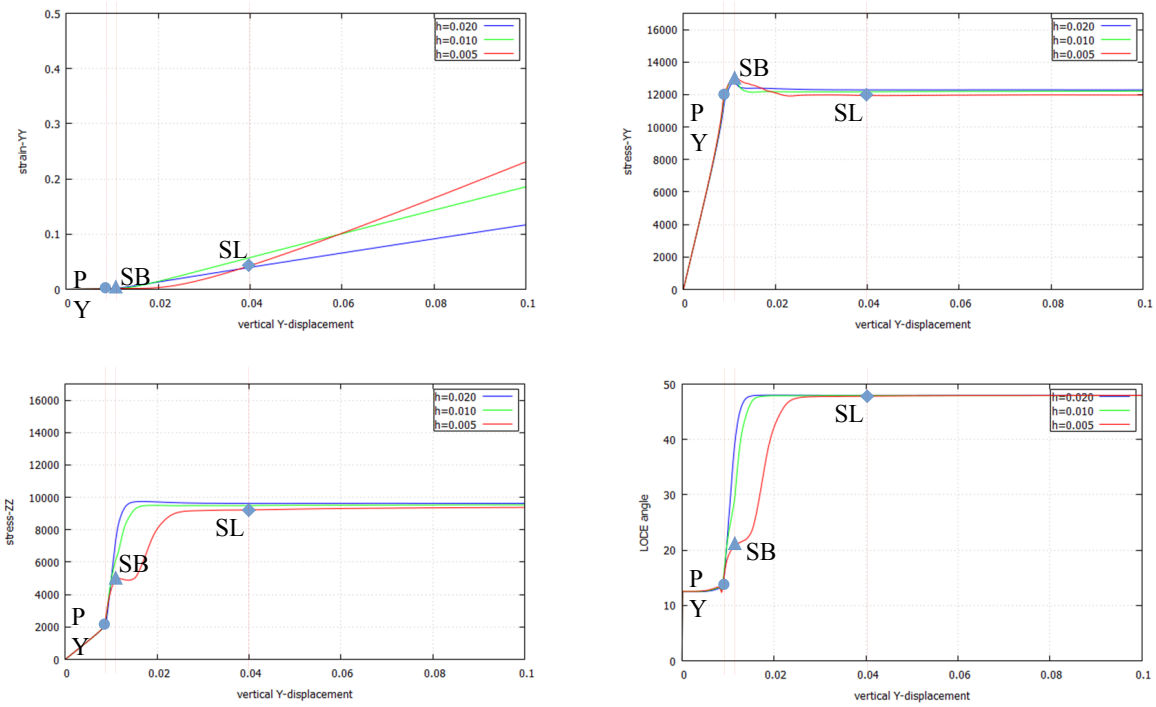

Figure 12: Strain, stresses and Lode angle of the non-associated von Mises/Hill model with Poisson's ratio $\nu_0 = 0.2$: Effects of the bandwidth

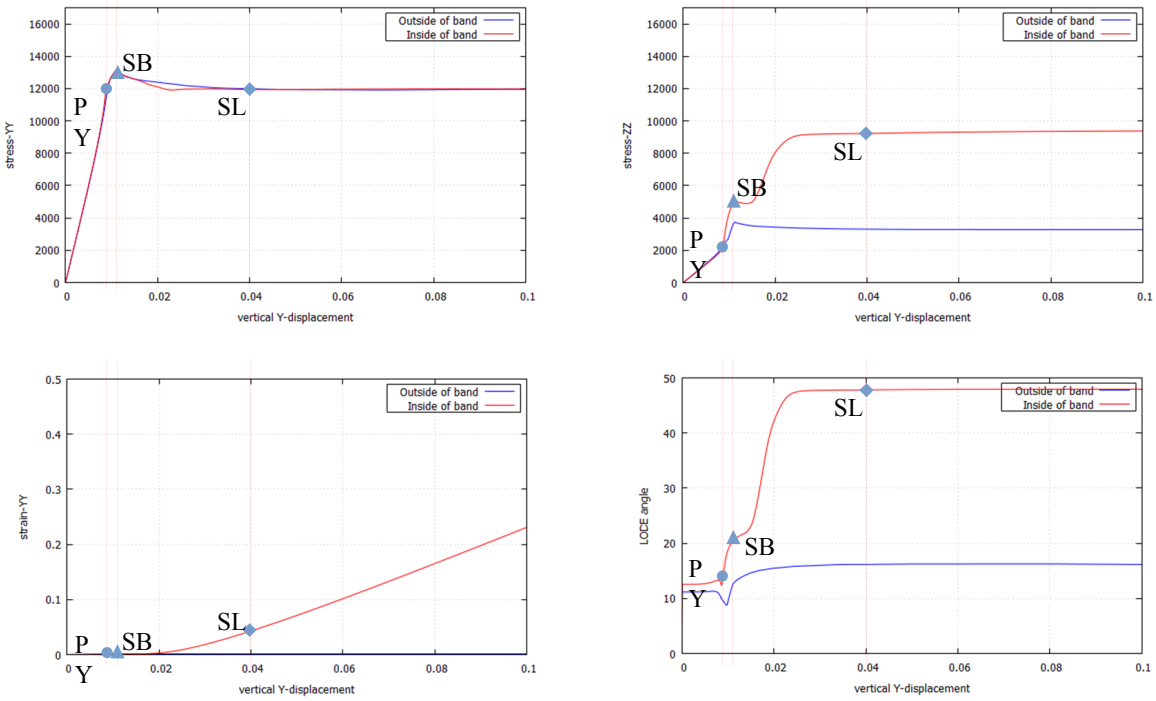

Figure 13: Evolution curves of the non-associated von Mises/Hill model with Poisson's ratio $\nu_0 = 0.2$.

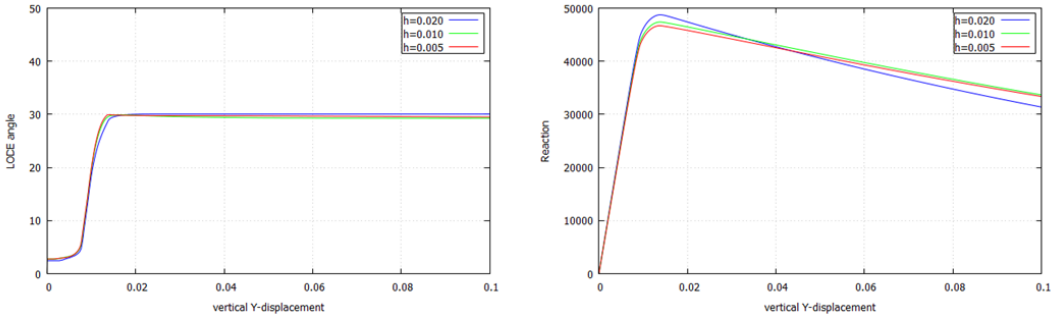

(a) Associated von Mises model with $\nu_0 = 0.0$

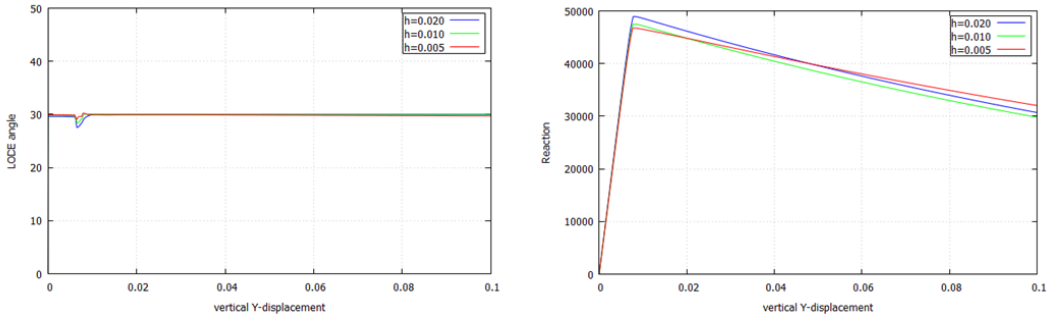

(b) Associated von Mises model with $\nu_0 = 0.5$

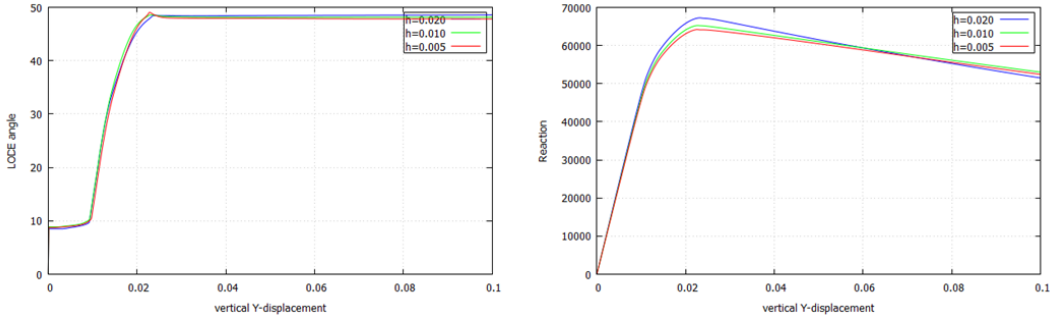

(c) Associated Hill model with $\nu_0 = 0.2$

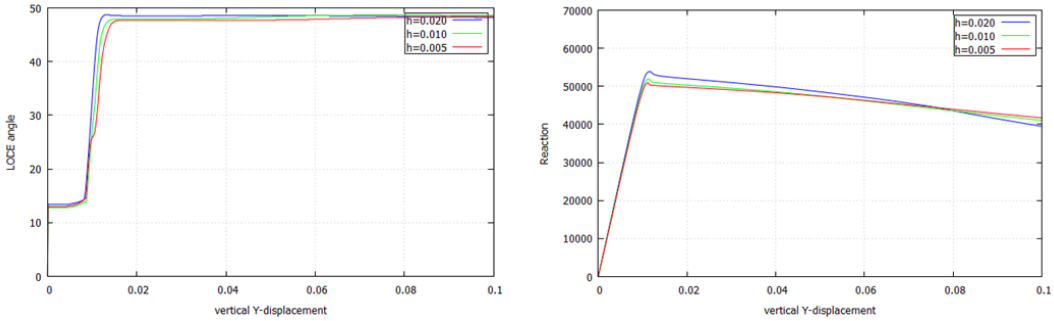

(d) Non-associated von Mises/Hill model with $\nu_0 = 0.2$

Figure 14: Evolution curves of Lode angle and vertical reaction for softening plasticity

For all the considered cases, the discontinuity bands form along as shown in Figure 5, along the 45° direction. Figure 14 shows the corresponding results. In the left column, the computed Lode angles for the elements inside the localization band are shown, corresponding exactly to the stress states that stem from satisfaction of the localization condition, i.e., 30° for the isotropic von Mises potential function and 47.78° for the Hill potential function. Note the resemblance to the corresponding results for the case of perfect plasticity shown in Figure 6, 8, 10 and 12, respectively. In the right column, the global vertical reaction — displacement curves are shown; in all cases, the softening responses and the convergence upon mesh refinement are observed.

5. Numerical examples

In this section, two extra numerical examples are presented to further validate the obtained strain localization condition under more general conditions.

5.1. The plane strain strip under uniaxial stretching

Firstly, the plane strain strip under uniaxial stretching presented in Section 4.2 is re-analyzed. Different from the previous simulations, here quadrilateral $\boldsymbol{u}/p$ elements are used to discretize the full computational domain. The mesh size is adopted as $h = 0.005$ m. In this way, two discontinuity bands that both satisfy the strain localization condition may form. Additionally, mesh alignment independence is also demonstrated for the discrete solution.

Four different models, i.e., the associated von Mises and Hill models, and the non-associated Hill/von Mises model (with the Hill criterion as the yielding function and the von Mises criterion as the potential one) and von Mises/Hill model (vice versa), are adopted in the simulation.

Let us first consider perfect plasticity. As mentioned before, for the case of no tilting, i.e., $\alpha = 0°$, the analytical results predict discontinuity bands of $\pm 45°$ directions for plastic models with either the von Mises or Hill potential function, and the yielding function does not alter the localization angle. The above results are exactly reproduced by the numerical simulations shown in Figure 15. It is worthy to note that even if the four final snapshots may look identical, they are not. The localization condition is identical for the four models, but the transition phases are different; distinct plastic strains accumulate during these phases. Minor differences can be observed around the horizontal slit, where plastic flows start.

Figure 16 presents three snapshots of the equivalent plastic strain at various applied displacements for the last model with the von Mises yielding function and the Hill potential one. The transition from plastic yielding/strain bifurcation to strain localization is evident, with the plastic strain evolving with increasing loading and the discontinuity angle eventually fixed at $\theta_\ell = 45°$. Let us recall that for the von Mises model, the strain bifurcation angle θ_b depends on Poisson's ratio, and $\theta_b > 45°$ for $\nu_0 < 0.5$ (Runesson et al., 1991).

Let us now consider the tilt angle $\alpha = 60°$. For the von Mises potential function, the flow tensor is isotropic and the same localization angles $\theta_\ell = \pm 45°$ apply. As shown in Figure 17(a) and Figure 17(b), the non-associated

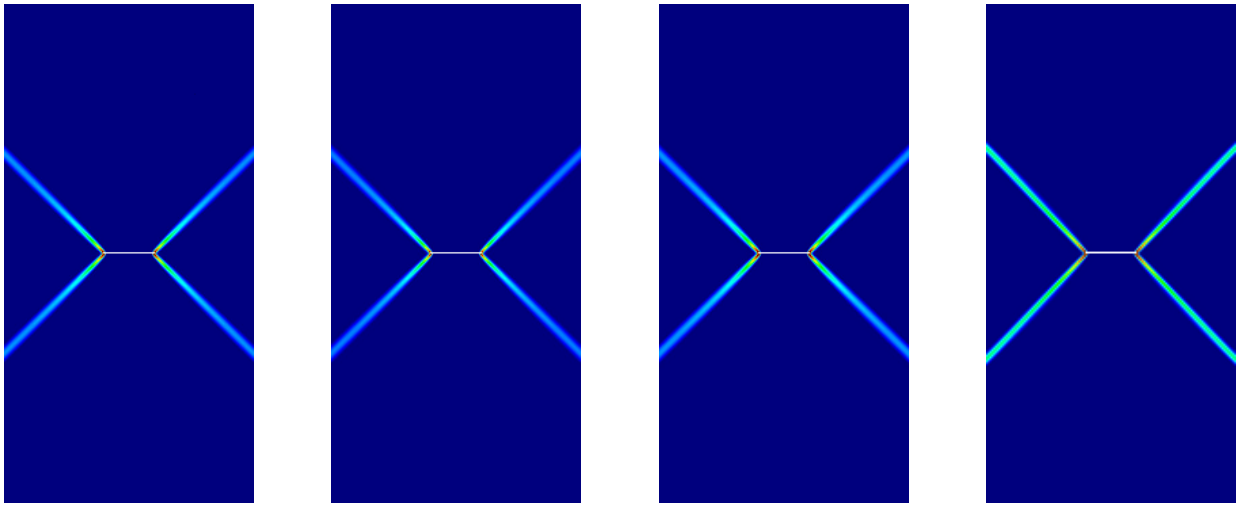

(a) von Mises model (b) Hill/von Mises model (c) Hill model (d) von Mises/Hill model

Figure 15: A plane strain strip under uniaxial stretching: Localization angles for various models with no tilting

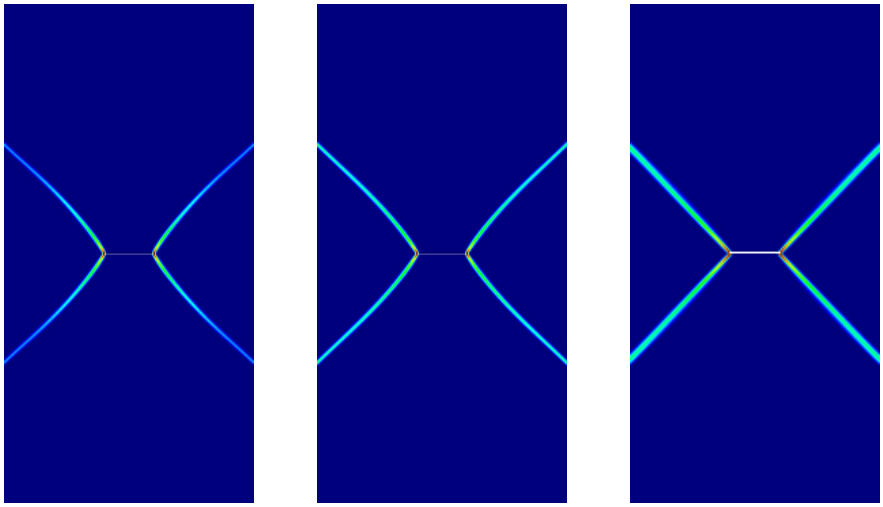

(a) $u^* = 0.010$ m (b) $u^* = 0.015$ m (c) $u^* = 0.030$ m

Figure 16: Snapshots of the equivalent plastic strain at various applied displacements, showing rotation of the discontinuity orientation for the non-associated von Mises/Hill model.

Hill/von Mises model shows the same localization as the associated von Mises model. The yield function does not alter the localization angle. Comparatively, for the Hill potential function, it follows from Eq. (4.16) that

$$\theta_\ell = -8.5^\circ;\ 81.5^\circ, \qquad \theta_\ell + \alpha = 51.5^\circ;\ 141.5^\circ \tag{5.1}$$

where $\theta_\ell + \alpha$ denotes the slopes of the upper discontinuity bands. As can be seen from Figure 17(c) and Figure 17(d), the above analytical results are correctly predicted by the numerical simulations. Moreover, the non-associated von Mises/Hill model exhibits a localization pattern similar to that of the associated Hill model. Dependence of the

localization angles only on the plastic potential function regardless the yield one is again confirmed.

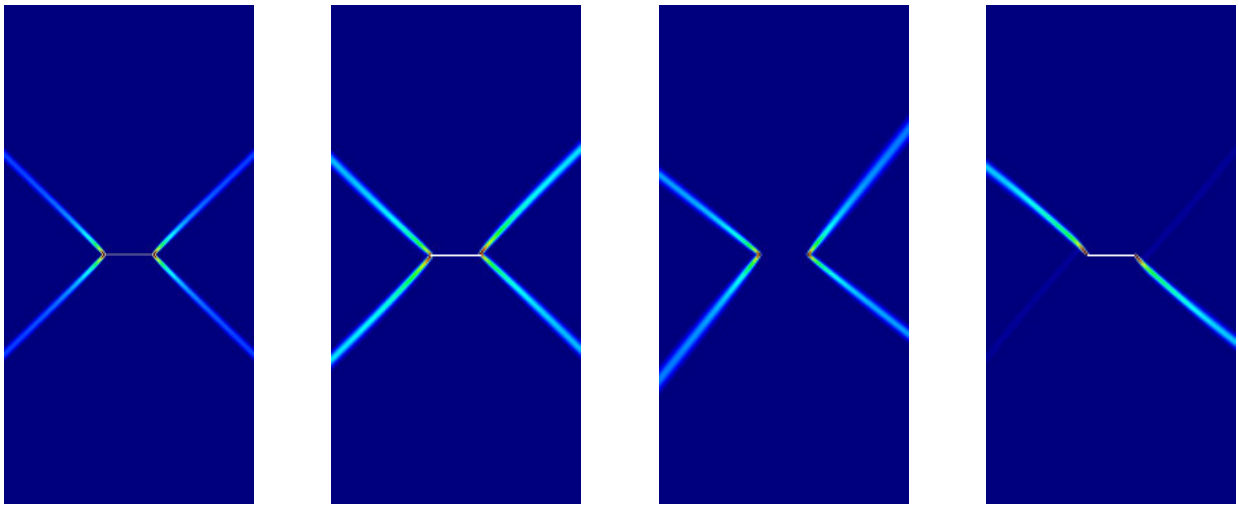

(a) von Mises model (b) Hill/von Mises model (c) Hill model (d) von Mises/Hill model

Figure 17: A plane strain strip under uniaxial stretching: Localization angles for various models with tilting angle $\alpha = 60°$.

Figure 18 presents three snapshots of the equivalent plastic strain at various applied displacements for the non-associated von Mises/Hill model. In this peculiar instance, the four initial symmetric plastic bands rotate during the transition phase until two of them eventually localize at an angle compatible with the localization condition while the other two, orthogonal to the former, progressively fade into desactivation. As mentioned previously, even if the localization conditions of cases (a) and (b), and cases (c) and (d), are identical respectively, the corresponding transition phases are not. This accounts for the slight curvature of the sliding lines in cases (b) and (d) around the slits.

Finally, let us consider softening plasticity. Figure 19 and Figure 20 show the discontinuity bands obtained for the non-associated von Mises/Hill model, for tilting angles (a) $\alpha = 0°$, (b) $\alpha = 60°$, respectively. The adopted softening properties are the same as in Section 4.2.5. The resemblance with the corresponding results for perfect plasticity, Figure 15(d) and Figure 17(d), respectively, is evident.

5.2. A plane strain punch test: Elasto- and rigid-plastic models

The second example is the punch indentation test by a flat rigid die shown in Figure 21. This is a well-known 2-D plane strain problem often used in the literature to test the ability of plastic models in capturing the failure modes. The problem was first studied by Prandtl (1920) for rigid-plastic bodies and then by Hill (1950) and Rice (1973) for elasto-plastic materials.

As the non-associated models have been discussed in the previous sections, only the associated von Mises and Hill models are considered. The reference material parameters adopted in the simulations are: Young's modulus $E_0 = 10$ MPa, Poisson's ratio $\nu_0 = 0.2$ and the yield strength $\sigma_Y = 10$ kPa for isotropic plasticity and $\sigma_{Y,11} = 15$ KPa with

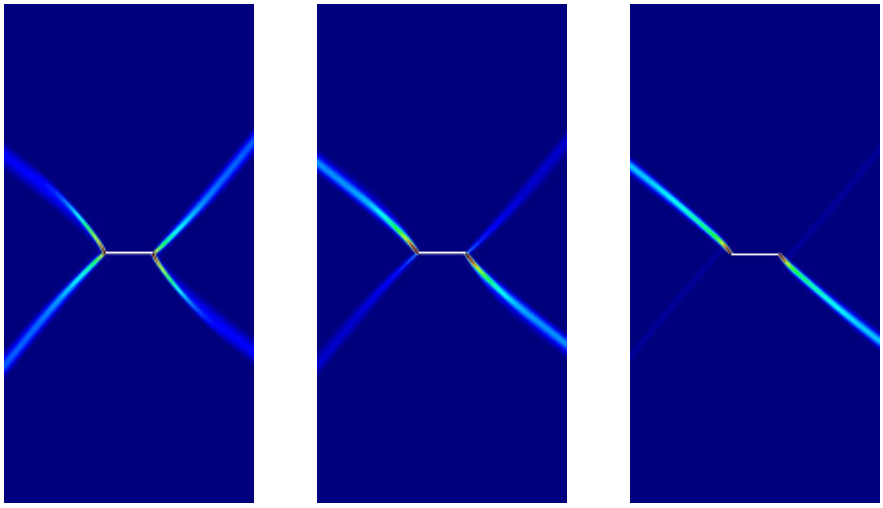

(a) $u^* = 0.010$ m (b) $u^* = 0.015$ m (c) $u^* = 0.030$ m

Figure 18: Snapshots of the equivalent plastic strain at various applied displacements, showing rotation of the discontinuity orientation for the non-associated von Mises/Hill model (with tilt angle $\alpha = 60°$).

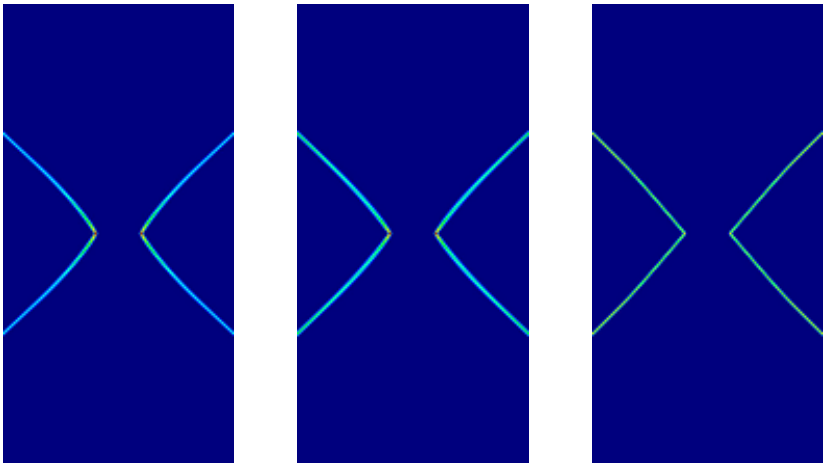

(a) $u^* = 0.010$ m (b) $u^* = 0.015$ m (c) $u^* = 0.030$ m

Figure 19: Snapshots of the equivalent plastic strain at various applied displacements, showing rotation of the discontinuity orientation for the softening non-associated von Mises/Hill model (with tilt angle $\alpha = 0°$).

all the others equal to 10 kPa for orthotropic ones (a tilt angle 60° is assumed for the material axes). Perfect plasticity is used.

Note that the material right under the rigid die is almost under uniaxial vertical loading in the global axes, i.e., $\sigma_{xy} = 0$; similarly, the material around the top surface (not under the die) is subjected to uniaxial horizontal stresses; see Figure 22. Therefore, the analytical results given in Eq. (5.1) apply here, with the localization angle depending only on the tilt of the material axes and the potential function.

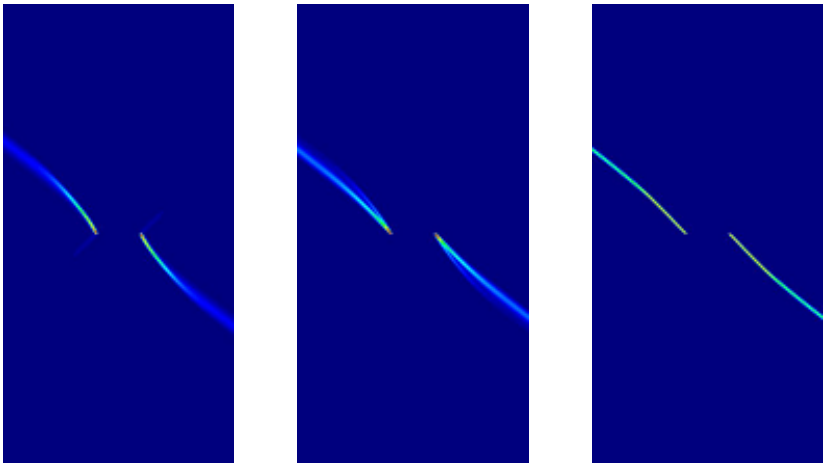

(a) $u^* = 0.010$ m (b) $u^* = 0.015$ m (c) $u^* = 0.030$ m

Figure 20: Snapshots of the equivalent plastic strain at various applied displacements, showing rotation of the discontinuity orientation for the softening non-associated von Mises/Hill model (with tilt angle $\alpha = 60°$).

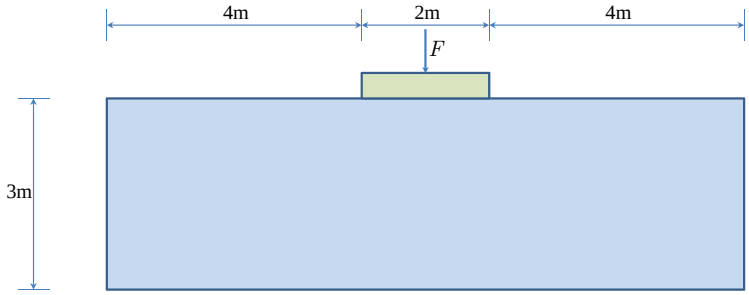

Figure 21: Indentation by a flat rigid die: Dimensions and loading. The bottom edge is fixed in both direction, while the left and right edges are constrained horizontally.

5.2.1. Rough punch: Prandtl's solution

A rough punch is first studied; that is, the material directly under the punch is not allowed to move horizontally, corresponding to so-called Prandtl's solution.

We first consider the associated elasto-plastic models. As shown in Figure 23, the localization angle under the footing and close to the free surface is fixed $\theta^{\mathrm{cr}} = \pm 45°$ with respect to the material axes, whatever the plastic yield function is. It is worth noting that the failure modes correspond to the claimed Prandtl's solution for rigid-plastic models. This coincidence confirms the the analytical prediction that rigid-plastic and elasto-plastic failure follow similar mechanics.

As demonstrated in Hill (1950), the failure mode is completely independent from the elastic constants. In the following, independence from the magnitude of the elastic modulus is shown. To this end, the analysis are performed with various values of Young's modulus, ranging three orders of magnitude. The computed load – displacement curves

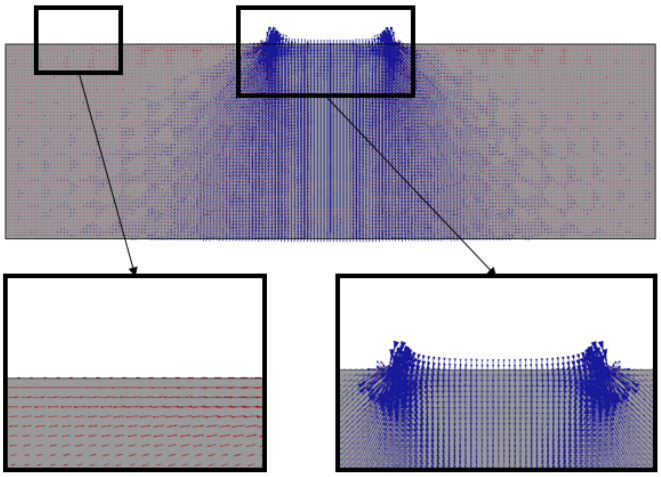

Figure 22: Indentation by a flat rigid die: Directions of principal stresses around the rigid footing.

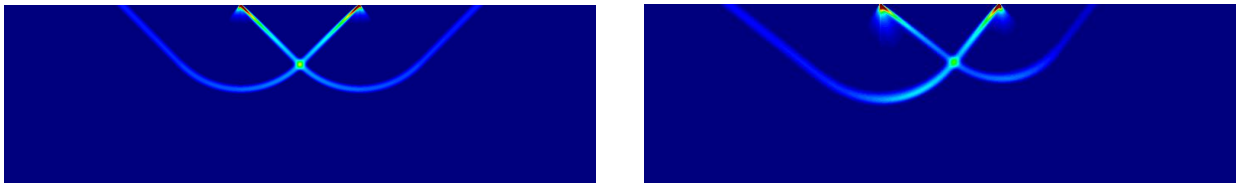

(a) Associated von Mises model

(b) Associated Hill model

Figure 23: Indentation by a flat rigid die (rough punch): Localization angles for the associated von Mises and Hill models with tilting angle $\alpha = 60°$.

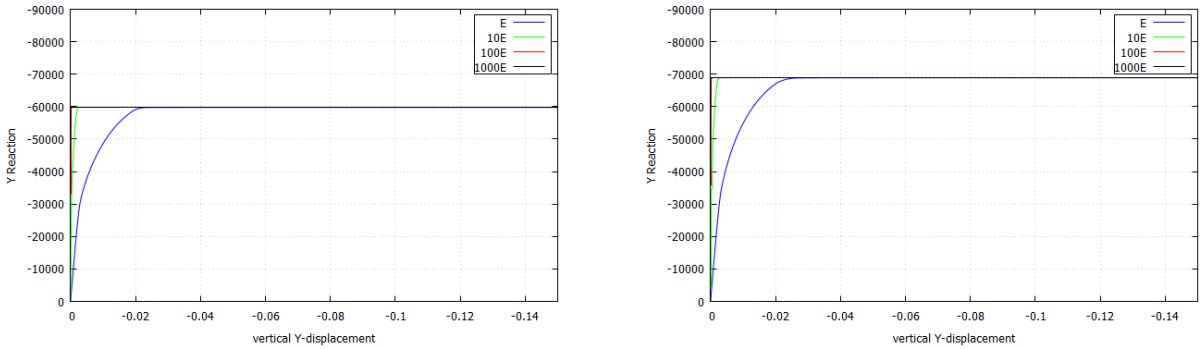

(a) Associated von Mises model

(b) Associated Hill model

Figure 24: Indentation by a flat rigid die: Load – displacement curves for the associated von Mises and Hill models with tilting angle $\alpha = 60°$.

are shown in Figure 24. As can be seen, the global response is progressive stiffer, but the failure loads are identical as predicted analytically. The corresponding failure modes are exactly identical. Moreover, the stiffer the material, the

shorter the transition phase appears to be.

Finally, Figure 25 shows the discontinuity bands obtained for the associated von Mises and Hill models with the tilting angle $\alpha = 60°$, when softening plasticity is considered. The same softening properties as in Section 4.2.5 are adopted. The failure mechanisms are identical to those corresponding to perfect plasticity. Figure 26 shows the computed load–displacement curves for progressively increasing Young's moduli. As can be seen, the global response is stiffer, but failure mechanisms and the softening branches are unaffected.

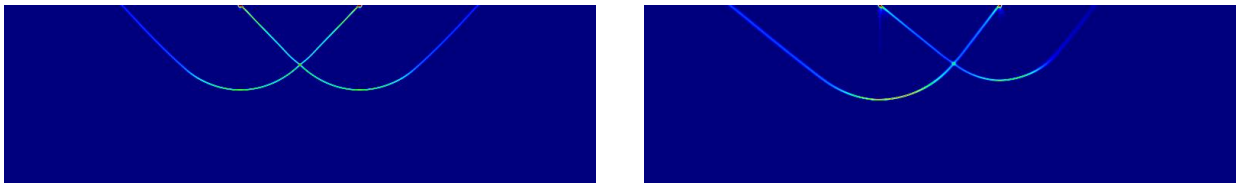

(a) Associated von Mises model

(b) Associated Hill model

Figure 25: Indentation by a flat rigid die (rough punch): Localization angles for the softening associated von Mises and Hill models with tilting angle $\alpha = 60°$.

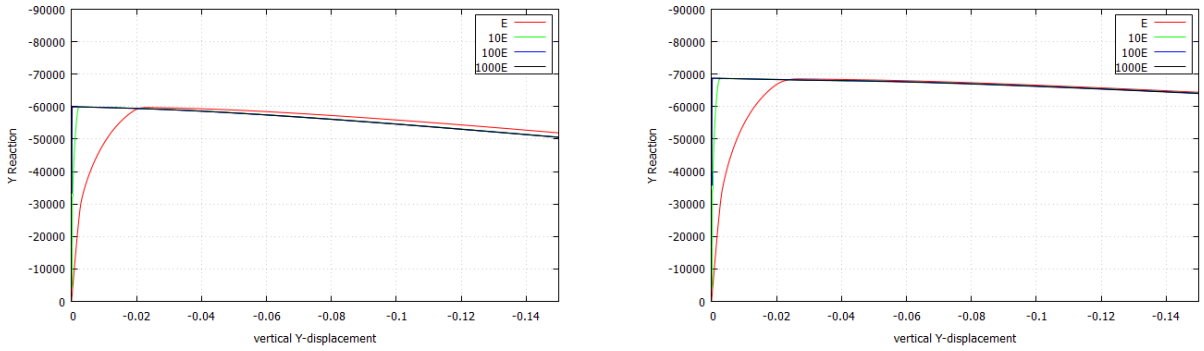

(a) Associated von Mises model

(b) Associated Hill model

Figure 26: Indentation by a flat rigid die: Load – displacement curves for the softening associated von Mises and Hill models with tilting angle $\alpha = 60°$.

Remark 5.1 For the von Mises rigid-plastic model, the limit load is given by (Hill, 1950)

$$F = 2a\frac{\sigma_Y}{\sqrt{3}}(\pi + 2) = 59370 \text{ N} \tag{5.2}$$

for $a = 1$ m here, coincident with the numerical predictions. □

5.2.2. Smooth punch: Hill's solution

A smooth punch is now investigated; that is, the material points locating directly under the punch are allowed to move horizontally. The only difference from the previous rough case is the boundary conditions at the base of the punch.

The corresponding failure patterns for the associated von Mises and the Hill models are shown in Figure 27. The former one corresponds to so-called Hill's solution for the punch problem (Hill, 1950).

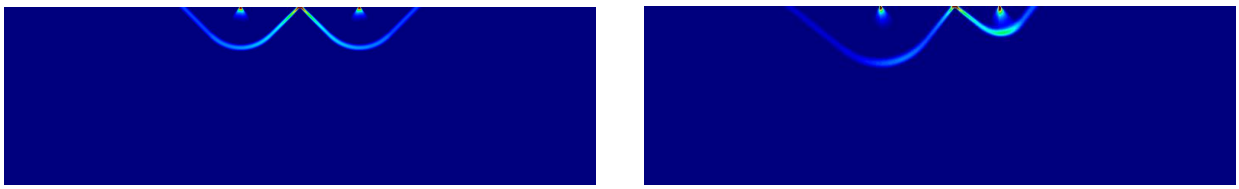

(a) Associated von Mises model

(b) Associated Hill model

Figure 27: Indentation by a flat rigid die (smooth punch): Localization angles for the associated von Mises and Hill models with tilting angle $\alpha = 60°$.

It can be seen that in these new solutions, the localization angles under the footing and close to the free surface are also fixed as $\theta^{\text{cr}} = \pm 45°$ with respect to the material axes.

Remarkably, the analytical and numerical load capacities of these solutions are exactly the same as those obtained for the rough punch. Additionally, the failure modes and load are independent from the elastic moduli and apply both to elasto-plastic and rigid-plastic materials.

This last example illustrates that the localization condition applies locally, but the formation of global failure modes depends crucially on the global equilibrium and the kinematic boundary conditions. These are the basis of classical plastic limit analyses.

6. Conclusions

In this work the mechanics of strain localization is addressed both analytically and numerically for isotropic and orthotropic, elasto- and rigid-plastic solids with associated or non-associated flow laws. More specifically, we postulated the stress (rate) objectivity (i.e., independent of the discontinuity bandwidth) as the necessary condition for the occurrence of strain localization, in addition to Maxwell's kinematics and continuity of the traction (rate) for strain bifurcation. Consequently, strain localization is more demanding than the classical continuous/discontinuous strain bifurcation, though both accounts for the plastic loading/unloading and loading/loading scenarios. For the plane strain condition, there generally exists a transition stage between plastic yielding/strain bifurcation and strain localization. Moreover, regarding the stress (rate) within the discontinuity band, the boundedness condition (Oliver, 1996, 2000; Cervera et al., 2012) and the continuity condition (Wu and Cervera, 2014, 2015, 2016), both assuming plastic loading/unloading with associated evolution laws in strain softening solids, are recovered as particular cases of strong discontinuities with a vanishing bandwidth and of regularized ones with a finite bandwidth, respectively. The concept of "slip-line" or "zero rate of extension" is also incorporated for rigid-plastic solids (Hill, 1950) and soils (Roscoe, 1970).

The kinematic and static constraints upon strain localization were then derived analytically. In particular, the localization angles of the discontinuity band (surface) depend only on the specific stress state and the plastic flow tensor, relevant neither to the elastic material constants nor to the plastic yield function. During the transition stage the orientation of the discontinuity band (surface) rotates progressively to the localization angle. For the plane strain condition, the yield function affects evolution process upon which the out-of-plane stress for strain localization is achieved and consequently the transition stage, but not the localization angle.

The above strain localization condition and analytical results for the localization angle are validated numerically by several benchmark examples. The stabilized mixed finite element formulation is adopted to deal with the quasi-incompressible deformations resulting from the von Mises and Hill potential functions. It is found that for perfectly and softening plastic solids with either associated or non-associated evolution laws, upon strain localization and thereafter the stresses inside the discontinuity band are indeed independent of the bandwidth, validating the postulated assumption. Moreover, similarly to our previous work on plastic or damaging solids, the numerically predicted localization angles are coincident with those given by the analytical results, further justifying the proposed strain localization condition.

As it applies to isotropic and orthotropic rigid-/elasto-plastic solids with associated or non-associated flow rules, the proposed strain localization condition can be used to determine the discontinuity orientation in the numerical modeling of localized failure in solids. In particular, it would be very helpful to track crack propagation paths, which is a challenging and open issue in the discontinuous approach like extended or enriched finite element methods (Wu, 2011; Wu et al., 2015; Wu and Li, 2015); see Zhang and Zhuang (2018); Zhang et al. (2021); Benvenuti and Orlando (2021a). This will be explored in forthcoming jobs.

Acknowledgments

Financial support from the Spanish Government-MINECO-Proyectos de I + D (Excelencia)-DPI2017-85998-P-ADaMANT-Computational Framework for Additive Manufacturing of Titanium Alloy, the Severo Ochoa Programme for Centres of Excellence in R&D (CEX2018-000797-S) and the Catalan Government – ACCIÓ - Ris3cat Transport and PRO^2 Project is gratefully acknowledged as well as the support of the Agència de Gestió d'Ajuts Universitaris i de Recerca (AGAUR) and the European Social Fund (ESF) to S. Kim through the predoctoral FI grants (ref. num. 2019FI-B00727). This work is also supported by National Natural Science Foundation of China (52125801; 51878294), National Key Laboratory of Shockwave and Denotation Physics (JCKYS2020212016) and Guangdong Provincial Key Laboratory of Modern Civil Engineering Technology (2021B1212040003) to J.Y. Wu.

References

Banabic, D., Kami, A., Comsa, D.S., Eyckens, 2021. Developments of the marciniak-kuczynski model for sheet metal formability: A review. Journal of Materials Processing Tech. 287, 116446.

Benallal, A., Comi, C., 1996. Localization analysis via a geometrical method. Int. J. Solids Structures 33, 99–119.

Benvenuti, E., Orlando, N., 2021a. A mesh-independent framework for crack tracking in elastodamaging materials through the regularized extended finite element method. Computational Mechanics 68, 25–49.

Benvenuti, E., Orlando, N., 2021b. Modeling mixed mode cracking in concrete through a regularized extended finite element formulation considering aggregate interlock. Engineering Fracture Mechanics 258, 108102.

Benvenuti, E., Tralli, A., Ventura, G., 2008. A regularized xfem model for the transition from continuous to discontinuous displacements. Int. J. Numer. Meth. Engng. 74, 911–944.

Borré, G., Maier, G., 1989. On linear versus nonlinear flow rules in strain localisation analysis. Meccanica 24, 36–41.

Brezzi, F., Fortin, M., 1991. Mixed and Hybrid Finite Element Methods. Springer, Berlin.

Cervera, M., Chiumenti, M., 2009. Size effect and localization in j_2 plasticity. International Journal of Solids and Structures 46, 3301–3312.

Cervera, M., Chiumenti, M., Benedetti, L., Codina, R., 2015. Mixed stabilized finite element methods in nonlinear solid mechanics. part iii: Compressible and incompressible plasticity. Comput. Methods Appl. Mech. Eng. 285, 752–775.

Cervera, M., Chiumenti, M., Di Capua, D., 2012. Benchmarking on bifurcation and localization in j_2 plasticity for plane stress and plane strain conditions. Comput. Methods Appl. Mech. Eng. 241–244, 206–224.

Cervera, M., Chiumenti, M., de Saracibar, C.A., 2003a. Softening, localization and stabilization: capture of discontinuous solutions in j2 plasticity. Int. J. Numer. Anal. Methods Geomech. 28, 373–393.

Cervera, M., Chiumenti, M., de Saracibar, C.A., 2004. Shear band localization via local j2 continuum damage mechanics. Comput. Method Appl. Mech. Eng. 193, 849–880.

Cervera, M., Chiumenti, M., Valverde, Q., de Saracibar, C.A., 2003b. Mixed linear/linear simplicial elements for incompressible elasticity and plasticity. Computer Methods in Applied Mechanics and Engineering 192, 5249–5263.

Cervera, M., Agelet de Saracibar, C., Chiumenti, M., 2002. COMET: COupled MEchanical and Thermal analysis. Data Input Manual, Version 5.0. Technical Report Technical Report IT-308. CIMNE, Technical University of Catalonia. Available from: http://www.cimne.upc.es.

Cervera, M., Wu, J.Y., Chiumenti, M., Kim, S., 2020. Strain localization analysis of hill's orthotropic elastoplasticity: analytical results and numerical verification. Computational Mechanics 65, 533–554.

Chiumenti, M., Valverde, Q., de Saracibar, C.A., Cervera, M., 2002. A stabilized formulation for incompressible elasticity using linear displacement and pressure interpolations. Computer Methods in Applied Mechanics and Engineering 191, 5253–5264.

Chiumenti, M., Valverde, Q., de Saracibar, C.A., Cervera, M., 2004. A stabilized formulation for incompressible plasticity using linear triangles and tetrahedra. Int. J. Plasticity 20, 1487–1504.

CIMNE, 2009. Gid: The personal pre and post processor Available from: http://www.gidhome.com.

Codina, R., 2000. Stabilization of impressibility and convection through orthogonal sub-scales in finite element methods. Comput. Method Appl. Mech. Eng. 190, 1579–1599.

Codina, R., Blasco, J., 1997. A finite element method for the stokes problem allowing equal velocity-pressure interpolations. Comput. Method Appl. Mech. Eng. 143, 373–391.

Hencky, H., 1923. Über einige statisch bestimmte fälle des gleichgewichts in plastischen körpern. Z. Angew. Math. Mech. 3, 241–251.

Hencky, H., 1924. Zur theorie plastischer deformationen und der hierdurch im material hervorgerufenen nachspannungen. Z. Angew. Math. Mech. 4, 323–334.

Hill, R., 1948. A theory of the yielding and plastic flow of anisotropic metals. Proc. Roy. Soc. A 193, 281–297.

Hill, R., 1950. The Mathematical Theory of Plasticity. Oxford University Press, New York.

Hill, R., 1958. General theory of uniqueness and stability of elasto-plastic solids. J. Mech. Phys. Solids 6, 236–249.

Hill, R., 1962. Acceleration waves in solids. J. Mech. Phys. Solids 10, 1–16.

Hughes, T., 1995. Multiscale phenomena: Green's function, dirichlet-to neumann formulation, subgrid scale models, bubbles and the origins of stabilized formulations. Comput. Method Appl. Mech. Eng. 127, 187–401.

Hughes, T., Feijoó, G., Mazzei, L., Quincy, J., 1998. The variational multiscale method – a paradigm for computational mechanics. Comput. Method Appl. Mech. Eng. 166, 3–28.

Kim, S., Cervera, M., Wu, J.Y., Chiumenti, M., 2021. Strain localization of orthotropic elasto–plastic cohesive–frictional materials: Analytical results and numerical verification. Materials 14, 2040.

Li, M., Füssl, J., Lukacevic, M., Eberhardsteiner, J., 2018. A numerical upper bound formulation with sensibly-arranged velocity discontinuities and orthotropic material strength behavior. Journal of Theoretical and Applied Mechanics 56, 417–433.

Lumelskyj, D., Rojek, J., Lazarescu, L., Banabic, D., 2019. Determination of forming limit curve by finite element method simulations. Procedia Manufacturingrocedia Manufacturing 27, 78–82.

Mandel, J., 1942. Equilibre par trasches planes des solides à la limite d'écoulement. Ph.D. thesis. Thèse, Paris.

Marciniak, Z., Kuczyński, K., 1967. Limit strains in the processes of stretch-forming sheet metal. Int. J. Mech. Sci. 9, 609–620.

Martínez-Pañeda, E., Betegón, C., 2015. Modeling damage and fracture within strain-gradient plasticity. International Journal of Solids and Structures 59, 208–215.

Mohr, O., 1900. Welche umstande bedingen der bruch und der elasizitätsgrenze des materials. Z. Verins Deutscher Ingenieure , 1524.

Oliver, J., 1996. Modeling strong discontinuities in solid mechanics via strain softening constitutive equations. part i: Fundamentals; part ii: Numerical simulation. International Journal for Numerical Methods in Engineering 39, 3575–3600; 3601–3623.

Oliver, J., 2000. On the discrete constitutive models induced by strong discontinuity kinematics and continuum constitutive equations. International Journal of Solids and Structures 37, 7207–7229.

Oliver, J., Cervera, M., Manzoli, O., 1999. Strong discontinuities and continuum plasticity models: the strong discontinuity approach. Int. J. Plast. 15, 319–351.

Oliver, J., Huespe, A.E., Dias, I.F., 2012. Strain localization, strong discontinuities and material fracture: Matches and mismatches. Comput. Methods Appl. Mech. Eng. 241-244, 323–336.

Ottosen, N., Runesson, K., 1991. Discontinuous bifurcation in a nonassoicated mohr material. Mechanics of Materials 12, 255–265.

Poh, L., Swaddiwudhipong, S., 2009. Over-nonlocal gradient enhanced plastic-damage model for concrete. Int. J. Solids Structure 46, 4369–4378.

Prandtl, L., 1920. Über die häete plastistischer körper. Nachr. Ges. Wisensch, Göttingen, math. phys. Klasse , 74–85.

Rice, J., 1976. The localisation of plastic deformations, in: Koiter, W. (Ed.), Theoretical and Applied Mechanics, North-Holland, Amsterdam. pp. 207–220.

Rice, J.R., 1968. A path independent integral and the approximate analysis of strain cncentrations by notches and cracks. J. Appl. Mech.-T. ASME 35, 379–386.

Rice, J.R., 1973. Plane strain slip line theory for anisotropic rigid/plastic materials. J. Mech. Phys. Solids 21, 63–74.

Rice, J.R., Rudnicki, J.W., 1980. A note on some features of the theory of localization of deformation. Int. J. Solids Structures 16, 597–605.

Rojek, J., Kleiber, M., Piela, A., Stocki, R., Knabel, J., 2004. Deterministic and stochastic analysis of failure in sheet metal forming operations. Steel Grips, Suppl. Matal Forming 2, 29–34.

Roscoe, K., 1970. The influence of strains in soil mechanics. Géotechnique 20, 129–170.

Rudnicki, J.W., Rice, J.R., 1975. Conditions of the localization of deformation in pressure-sensitive dilatant material. J. Mech. Phys. Solids 23, 371–394.

Runesson, K., Ottosen, N., Peric, D., 1991. Discontinuous bifurcations of elastic-plastic solutions at plane stress and plane strain. Int. J. Plast. 7, 99–121.

Simó, J., Hughes, T., 1998. Computational inelasticity. Springer, New York.

Simó, J., Oliver, J., Armero, F., 1993. An analysis of strong discontinuities induced by strain-softening in rate-independent inelastic solids. Comput. Mech. 12, 277–296.

Thomas, T., 1961. Plastic Flow and Fracture of Solids. Academic Press, New York.

Wu, J.Y., 2011. Unified analysis of enriched finite elements for modeling cohesive cracks. Comput. Methods Appl. Mech. Engrg. 200, 3031–3050.

Wu, J.Y., 2017. A unified phase-field theory for the mechanics of damage and quasi-brittle failure in solids. Journal of the Mechanics and Physics of Solids 103, 72–99.

Wu, J.Y., 2018a. A geometrically regularized gradient-damage model with energetic equivalence. Comput. Methods Appl. Mech. Engrg. 328, 612–637.

Wu, J.Y., Cervera, M., 2014. Strain localization and failure mechanics for elastoplastic damage solids. Monograph CIMNE M147, Barrcelona, Spain.

Wu, J.Y., Cervera, M., 2015. On the equivalence between traction- and stress-based approaches for the modeling of localized failure in solids. Journal of the Mechanics and Physics of Solids 82, 137–163.

Wu, J.Y., Cervera, M., 2016. A thermodynamically consistent plastic-damage framework for localized failure in quasi-brittle solids: Material model and strain localization analysis. International Journal of Solids and Structures 88-89, 227–247.

Wu, J.Y., Cervera, M., 2017. Strain localization of elastic-damaging frictional-cohesive materials: Analytical results and numerical verification. Materials 10, 434; doi:10.3390/ma10040434.

Wu, J.Y., Li, F.B., 2015. An improved stable xfem (is-xfem) with a novel enrichment function for the computational modeling of cohesive cracks. Comput. Methods Appl. Mech. Engrg. 295, 77–107.

Wu, J.Y., Li, F.B., Xu, S.L., 2015. Extended embedded finite elements with continuous displacement jumps for the modeling of localized failure in solids. Comput. Methods Appl. Mech. Engrg. 285, 346–378.

Wu, J.Y., Nguyen, V.P., 2018. A length scale insensitive phase-field damage model for brittle fracture. Journal of the Mechanics and Physics of Solids 119, 20–42.

Wu, J.Y., Nguyen, V.P., Nguyen, C.T., Sutula, D., Sinaie, S., Bordas, S., 2020. Phase field modeling of fracture. Advances in Applied Mechancis: Fracture Mechanics: Recent Developments and Trends volume 53, 1–183; https://doi.org/10.1016/bs.aams.2019.08.001.

Zhang, Y., Huang, J., Yuan, Y., Mang, H.A., 2021. Cracking elements method with a dissipation-based arc-length approach. Finite Elements in Analysis and Design 195, 103573.

Zhang, Y., Zhuang, X., 2018. Cracking elements: A self-propagating strong discontinuity embedded approach for quasi-brittle fracture. Finite Elements in Analysis and Design 144, 84–100.